231Pa and 230Th in the Arctic Ocean: Implications for boundary scavenging and 231Pa230Th fractionation in the Eurasian Basin

Sandra Gdaniec, Matthieu Roy-Barman, Martin Levier, Ole Valk, Michiel Rutgers van Der Loeff, Lorna Foliot, Arnaud Dapoigny, Lise Missiaen, Carl-Magnus Mörth, Per Andersson

1 **^{231}Pa and ^{230}Th in the Arctic Ocean: implications for Boundary**

2 **Scavenging and ^{231}Pa-^{230}Th fractionation in the Eurasian Basin**

3

4 Sandra Gdaniec[a,b,c], Matthieu Roy-Barman[c], Martin Levier[c], Ole Valk[d], Michiel Rutgers van
5 der Loeff[d], Lorna Foliot[c], Arnaud Dapoigny[c], Lise Missiaen[c,*], Carl-Magnus Mörth[a], Per S.
6 Andersson[b]
7
8 [a] Stockholm University, Department of Geological Sciences, Stockholm, Sweden

9 [b] Swedish Museum of Natural History, Department of Geosciences, Stockholm, Sweden

10 [c] Laboratoire des Sciences du Climat et de l'Environnement, LSCE/IPSL, CEA-CNRS-UVSQ

11 Université Paris-Saclay, Gif-sur-Yvette, France

12 [d] Alfred Wegener Institute, Helmholtz Centre for Polar and Marine Research, Bremerhaven, Germany

13 *Present address: Climate Change Research Centre, University of New South Wales, Sydney,
14 Australia
15
16
17
18 Corresponding Author:
19 Sandra Gdaniec
20 Sandra.gdaniec@nrm.se
21 Frescativägen 40
22 114 18 Stockholm, Sweden
23
24
25
26 **Email addresses:** sandra.gdaniec@nrm.se (S. Gdaniec), matthieu.roy-barman@lsce.ipsl.fr
27 (M. Roy-Barman), ole.valk@awi.de (O. Valk), mloeff@awi.de (M. Rutgers van der
28 Loeff),martin.levier@lsce.ipsl.fr (M. Levier), lorna.foliot@lsce.ipsl.fr (L. Foliot),
29 arnaud.dapoigny@lsce.ipsl.fr (A. Dapoigny), l.missiaen@unsw.edu.au (L. Missiaen),
30 magnus.morth@su.se, (C. Mörth), per.andersson@nrm.se (P. Andersson).
31
32
33
34

Abstract

^{231}Pa, ^{230}Th and ^{232}Th were analyzed in filtered seawater (n = 70) and suspended particles (n = 39) collected along a shelf-basin transect from the Barents shelf to the Makarov Basin in the Arctic Ocean during GEOTRACES section GN04 in 2015. The distribution of dissolved ^{231}Pa and ^{230}Th in the Arctic Ocean deviates from the linear increase expected from reversible scavenging. Higher ^{232}Th concentrations were observed at the shelf, slope and in surface waters in the deep basin, pointing at lithogenic sources. Fractionation factors ($F_{Th/Pa}$) observed at the Nansen margin were higher compared to $F_{Th/Pa}$ in the central Nansen Basin, possibly due to the residual occurrence of hydrothermal particles in the deep central Nansen Basin. Application of a boundary scavenging model quantitatively accounts for the dissolved and particulate ^{230}Th distributions in the Nansen Basin. Modeled dissolved ^{231}Pa distributions were largely overestimated, which was attributed to the absence of incorporation of water exchange with the Atlantic Ocean in the model. ^{231}Pa/^{230}Th ratios of the suspended particles of the Nansen Basin were below the ^{231}Pa/^{230}Th production ratio, but top-core sediments of the Nansen margin and slope have high ^{231}Pa/^{230}Th-ratios, suggesting that scavenging along the Nansen margin partly acts as a sink for the missing Arctic ^{231}Pa.

1 Introduction

Particle reactive isotopes in the natural uranium and thorium decay series are useful tracers of particle flux and scavenging in the oceans (e.g. Edmonds et al., 2004; Roy-Barman, 2009; Rutgers van der Loeff and Berger, 1993). In seawater, ^{231}Pa and ^{230}Th are produced at a constant rate by the decay of homogeneously distributed ^{235}U and ^{234}U, respectively. Both ^{231}Pa and ^{230}Th are particle reactive elements, which means that they get scavenged onto settling particles and removed from the water column to the sediments. However, due to differences in their particle reactivity, the ^{231}Pa/^{230}Th ratio of seawater, marine particles and sediments often differs from that of the production ratio (Rutgers van der Loeff and Berger, 1993). The distribution and dispersion of ^{231}Pa and ^{230}Th in the water column and their ratio in sediments are of interest for processes controlling spatial and temporal variations in ocean biogeochemistry. The difference in the chemical behavior of the two tracers can result in large scale deviation of the ^{231}Pa/^{230}Th ratio of marine sediments compared to the production ratio of these nuclides in the overlying water column, with higher sedimentary ^{231}Pa/^{230}Th ratios at ocean margin and lower ^{231}Pa/^{230}Th to the inner ocean compared to the production ratio. Differences in particle concentration, composition and flux influence scavenging rates of ^{231}Pa and ^{230}Th in the water column (Chase et al., 2002). Environments governed by high particle flux, such as ocean margins are very effective sinks for ^{231}Pa and ^{230}Th (e.g. Scholten et al., 1995; Gdaniec et al., 2017). This process, usually referred to as boundary scavenging has previously been thought to be pronounced in the Arctic Ocean (Bacon et al., 1989; Cochran et al., 1995; Scholten et al., 1995). However, despite the contrasted particle fluxes over large shelf areas (receiving high river inputs) and the inner Arctic with its perennial sea ice cover, the ^{231}Pa/^{230}Th ratio of arctic sediment does not vary much and is on average lower than the production ratio (e.g. Edmonds et al., 2004; Moran et al., 2005b). Not many studies have reported ^{231}Pa/^{230}Th ratios slightly exceeding the production ratio (e.g. Luo and Lippold, 2015). The overall low ^{231}Pa/^{230}Th ratios casted some doubts on mechanisms driving the boundary scavenging in the Arctic Ocean. While boundary scavenging does occur in the Arctic Ocean (Roy-Barman, 2009), the net export of ^{231}Pa to the Atlantic Ocean through the Fram strait plays a key role in the Pa and Th budget of the Arctic Ocean (Edmonds et al., 2004; Hoffmann et al., 2013; Moran et al., 2005). However, the low vertical resolution, the relatively large analytical uncertainties and sometimes lack of particulate data limits the water column constraints on boundary scavenging in Arctic Ocean (Bacon et al., 1989; Cochran et al., 1995; Edmonds et al., 2004; Scholten et al., 1995) and more data are required for a proper modeling of boundary scavenging (Luo and Lippold, 2015).

In this study, dissolved and particulate ^{231}Pa, ^{230}Th, and ^{232}Th concentrations measured along GEOTRACES section GN04 in the Barents Sea, Nansen Basin, Amundsen

90   Basin and Makarov Basin are presented. The objective was to explore the influence of
91   boundary scavenging and shelf-basin interactions on the observed distribution of [231]Pa and
92   [230]Th in the Arctic Ocean. We revisit boundary scavenging modelling using a model adapted
93   from Roy-Barman (2009) that we compared to the current dataset and used to constrain the
94   scavenging behavior of Pa and Th between the Arctic margin and the inner ocean.
95

2. Methods

96

97   2.1 Sampling

98   Samples were collected on R/V Polarstern during expedition PS94 in 2015, at seven stations
99   located in the Barents Sea, Nansen, Amundsen and Makarov Basins along the GEOTRACES
100 GA04 section in the Arctic Ocean (Fig. 1). The samples were collected along a shelf-basin
101 transect from the Barents shelf to the Makarov Basin to study the exchange between the
102 margin and interior ocean. Stations 4, 161, 153 and 18 represent the shelf, station 32
103 represents the margin, while station 40, 50, 125 (Amundsen basin) and 101 (Makarov basin)
104 represent the interior ocean.
105   Water samples were collected in 24 L Niskin® bottles mounted on a General Oceanic®
106 rosette equipped with a Sea-Bird Electronics CTD system (SBE911plus). The CTD-system
107 was equipped with sensors allowing measurements of salinity, temperature and transmission
108 (Rabe et al., 2016; van Ooijen et al., 2016). For the analysis of dissolved [231]Pa, [230]Th and [232]Th,
109 5 L of water were filtered directly from the Niskin bottles into sampling containers using
110 Acropak500™ cartridges (0.45 µm pore size), which were cleaned in between stations. After
111 filtration, water samples were acidified using concentrated ultra-pure HCl (~1 ml of acid per 1
112 L of seawater). Samples were stored in double plastic bags until analysis.
113   Particulate samples were collected using *in-situ* pumps (McLane and Challenger
114 Oceanic) at six stations along the GA04 section (Fig. 1). Particles (0.8 µm pore size) were
115 collected on Supor® polyethersulfone filters with a diameter of 142 mm.
116   At two locations (N 84° 6´ 51.64", E 12° 4` 11.69" and N 84° 31.40", E 11° 6` 11.43"),
117 "dirty ice" (ice rafted sediments incorporated into sea ice when it forms on the Arctic shelf) was
118 collected from deck using a plastic spade and container.
119   At station 161, 32 and 101, surface sediment cores were collected using a Multi-corer
120 (Fig. 1). The top (0-1 cm interval) of each core was analyzed for [238]U, [234]U, [231]Pa, [232]Th and
121 [230]Th at LSCE.
122

123 2.2 Chemical preparation of Pa and Th in seawater, suspended particles, surface

124 sediments and dirty ice

125 ^{231}Pa, ^{230}Th and ^{232}Th were determined by isotope dilution and mass spectrometry. Seawater

126 samples were processed as described in (Gdaniec et al., 2017). For filtered particles,

127 approximately 1/5 (corresponding to ~25 - 200 L seawater) of the total filter material was cut

128 onboard in a laminar flow bench and used to determine the concentrations of ^{231}Pa and Th

129 isotopes in suspended particles. The leaching of filter samples was performed at the Swedish

130 Museum of Natural history followed by spiking and analysis at LSCE. The filters were

131 submerged in 3N HCl and heated to >50°C to wash the particles off the filters without dissolving

132 the filters. The leachate, containing the suspended particles, was then dissolved in a mixture

133 of concentrated HNO_3 and HF following the method described in Gdaniec et al. (2017).

134 Surface sediments were dried and an aliquot (0.2 g) of crushed bulk sediment was

135 spiked with ^{233}Pa, ^{229}Th and ^{236}U, followed by total dissolution in a HNO_3 and HF mixture. Pa,

136 Th and U were separated by anion exchange chromatography (Guihou et al., 2010).

137 The dirty ice samples were melted and particles were separated by centrifugation at

138 the clean laboratory of Laboratoire des Sciences de l'Environnement Marin (LEMAR). Total

139 dissolution of the particles (~0.2 g) was carried out at the Swedish Museum of Natural History

140 using microwave oven digestion using HF, HNO_3 and HCl followed by spiking, chemical

141 separation and analysis of ^{231}Pa, ^{230}Th and ^{232}Th at Laboratoire des Sciences du Climat et de

142 l´Environnement (LSCE).

143 ^{231}Pa, ^{230}Th and ^{232}Th concentrations in seawater, particles and sediment samples

144 were analyzed at LSCE by Multi Collector Inductively Coupled Plasma Mass Spectrometry

145 (MC-ICP-MS) on a Thermo Scientific™ Neptune Plus™ instrument equipped with an Aridus

146 II™ desolvating nebulizer and a Jet interface (Burckel et al., 2015, Gdaniec et al., 2017).

147 Uranium concentrations in seawater were estimated using the bottle salinity

148 measured from the CTD and the U-Salinity relationship in seawater (U = (0.100 * S – 0.326),

149 Owens et al., 2011). The conservative behavior of uranium in the Arctic Ocean can be

150 questioned due to the surface and mixed layer of the Arctic contain a significant portion of a

151 mixture of river and ice melt water. However, in the study of Not et al. (2012) the investigators

152 apply the U vs. salinity relationship over a salinity range of ~0 – 135, and showed that the U-

153 salinity relationship exhibits the conservative behavior over the entire range investigated.

154 Procedural blanks for seawater samples were determined by performing a complete

155 chemical procedure on 3-11 bottles of 250 ml of Milli-Q® water with each batch of samples.

156 Total procedural blanks for seawater samples ranged between 7.3 pg and 29.9 pg for ^{232}Th

157 (average = 15 ± 6 pg), 0.07 and 8.42 fg for ^{230}Th (average = 1.02 ± 1.80 fg) and 0.05 and 0.26

158 fg for ^{231}Pa (average = 0.17 ± 0.18 fg). These blanks were equivalent to 0.9 – 14 % of the

159 measured ^{232}Th, 0.2 – 21 % of the measured ^{230}Th and 0.1 – 42 % of the measured ^{231}Pa.

160   For particles, procedural blanks were prepared in the same way as for samples by

161 using acid cleaned filters (0.5N HNO$_3$) mounted onto the pump and deployed but not

162 connected to the pumping system. Total procedural blanks ranged between 3.3 pg and 29.1

163 pg for ^{232}Th (average = 4.3 ± 1.2 pg), 0.02 and 0.36 fg for ^{230}Th (average = 0.15 ± 0.03 fg) and

164 0.004 and 0.7 fg for ^{231}Pa (average = 0.27 ± 0.34 fg). These blanks were equivalent to 0.1 –

165 16 % of the measured ^{232}Th, 0.1 – 19 % of the measured ^{230}Th and 0.1 – 89 % of the measured

166 ^{231}Pa

167   All measured ^{231}Pa and ^{230}Th concentrations were corrected for the in-growth of ^{231}Pa

168 and ^{230}Th by uranium decay during the time period between sample collection and the U-Th/Pa

169 separation. All uncertainties are expressed as 2 standard errors on the mean (2 σ_n) including

170 the propagated contribution from sample weighting, spike impurities, spike contributions, blank

171 corrections and mass spectrometric measurements.

172 Replicates for dissolved ^{231}Pa, ^{230}Th and ^{232}Th concentrations were measured (Tab S1). It was

173 initiated because the first analysis of ^{230}Th at 1000 m depth for station 32 seemed obviously

174 overestimated. An additional aliquot of the 1000 m sample was analyzed and 2 additional

175 samples (500 m depth at St. 32 and 40) were replicated to check the method reliability. They

176 confirmed that the first analysis of ^{230}Th at 1000 m depth had suffered from contamination, but

177 showed a good agreement (within or close to analytical uncertainties) for the other ^{231}Pa and

178 ^{230}Th measurements. The ^{232}Th replicates can vary by as much as 30 % indicating small ^{232}Th

179 contaminations, but it will have no significant impact on the discussion.

180   An inter-comparison of dissolved and particulate Pa-Th measurements between

181 LSCE and AWI at stations 101 and 125 is given in Fig. ES1. Seawater samples at station 101

182 (GEOTRACES crossover station of the USCGC Healy HLY1502 (GN01) and R/V Polarstern

183 PS94 (GN04) cruises) and station 125 were duplicated and analyzed for dissolved ^{231}Pa, ^{230}Th

184 and ^{232}Th in order to provide an intercomparison between AWI and LSCE. These samples

185 were obtained from the same casts, but not always the same bottle, so some differences in

186 concentrations were expected (Fig. ES1). Concentrations of dissolved ^{231}Pa, ^{230}Th and ^{232}Th

187 at station 50 (Fig. 1) have been published in Valk et al., 2018 and will be used here to

188 investigate the relationship between the Nansen margin and interior. Moreover, an

189 intercomparison of dissolved and particulate Pa-Th measurements with AWI (Alfred Wegener

190 Institute), UMN (Minnesota University) and LDEO (Lamont Doherty Earth Observatory) at

191 station 101 is in progress.

192

193 3 Results

3.1 General circulation and Hydrography

The Arctic Mediterranean, like the Mediterranean Sea, transforms and exports Atlantic water of lower density entering from the adjacent ocean into high density intermediate and deep waters. The Arctic Ocean comprises two major basins, the Amerasian Basin and the Eurasian Basin, separated by the Lomonosov Ridge (Fig. 1). The Eurasian Basin is divided into the Nansen and Amundsen Basin by the Gakkel Ridge, while the Amerasian Basin is separated by the Alpha-Mendeleyev Ridge into the Makarov and the Canada Basins (Fig. 1).

The inflow of Atlantic Water (AW) over the Barents Sea was recognized at stations 161 and 153, where high salinity (>35.1) and high temperatures (~2 – 7.6°C) were observed (Rabe et al., 2016) (Fig. ES2). Close to the Barents Sea shelf break (St. 04 and 18), the polar waters (Polar Mixed Layer and Halocline) were significantly colder (≤ 0.8°C) and fresher (≤ 34.8) compared to the inflow of AW (Fig. ES2). AW enters the central Arctic Ocean mainly by two branches; the Fram Strait Branch Water (FSBW) and the Barents Sea Branch Water (BSBW) (Rudels, 1994). The FSBW enters the Nansen Basin through the Fram Strait and then forms the Boundary current that flows around the Nansen Basin along the Gakkel Ridge (e.g. Rudels, 2009) (Fig. ES3). As AW enters the Arctic Basin, it encounters sea ice and the upper water masses cool (-1.8°C) and become less saline (~34.9 - 35.0) compared to underlying waters (Fig. ES2).

The BSBW flows over the Barents Sea shelf and enters the Nansen Basin through St. Anna Trough (~1000 m depth), where limited exchange with FSBW occurs (e.g. Rudels, 2009) (Fig. ES3). At the eastern Siberian margin, the BSBW is divided into 3 branches: one branch flows into the Amundsen Basin while the second branch of the BSBW continues to flow towards the Fram Strait, as well as the ventilated intermediate water masses (Tanhua et al., 2009) (Fig. ES3). The third part of the BSBW prolongs into the Makarov Basin as part of the Arctic Ocean Boundary Current that travels anti-cyclonically around the Arctic Ocean (Rudels, 1994; Rudels et al., 2012).

In the Nansen Basin (St. 32 and 40), the warm FSBW was observed between ~100 and ~1000 m (Rabe et al., 2016) (Fig. ES2). In these waters, the Atlantic layer typically has maximum temperature of ~2.5°C and the salinity ranges between 34.9 and 35.05 (Fig. ES2). Station 50, in the central Nansen Basin is influenced by the return flow of colder (-2°C) and less saline FSBW along the Gakkel Ridge (Rabe et al., 2016) (Fig. ES2).

The Eurasian Basin communicates with the Canada Basin through the boundary current that enters the Canada Basin north of Siberia and through the intra-Basin located at the central part of the Lomonosov Ridge, with a sill depth of ~1850 m (Björk et al., 2007) (Fig. ES3). A reverse flow from the Makarov Basin to the Amundsen basin has also been identified (Björk et al., 2010, 2007)

230   Above 1700 m, stations 125 and 101 show similar water mass characteristics that fit

231   to the BSBW (Rabe et al., 2016) (Fig. ES2). Below this depth range, the deep waters of the

232   Amerasian Basin are warmer and saltier compared to the Eurasian Basin Deep Water (EBDW)

233   (Fig. ES2) (e.g. Aagaard et al., 1981).The deep waters from the Eurasian Basin exit the Arctic

234   through the Fram Strait and contribute to the deeper layers in the Nordic Seas (e.g. Rudels,

235   2015).

236   3.2 Dissolved and particulate ^{232}Th concentrations

237   Concentrations of dissolved ^{232}Th in the Arctic Ocean ranged between 11 and 205 pg/kg and

238   were generally decreasing with depth (Fig. 2). Elevated concentrations of ^{232}Th were observed

239   close to the Nansen shelf break at station 04 and 18 (72 – 205 pg/kg) and in surface waters of

240   station 101 (139 –194 fg/kg). Below ~500m depth, concentrations of dissolved ^{232}Th were

241   higher closer to the Nansen margin (24 – 80 pg/kg) compared to the Nansen interior (11 – 60

242   pg/kg) (Fig. 2).

243   Concentrations of particulate ^{232}Th in the Barents Sea display elevated concentrations

244   at depth, where concentrations up to ~2500 pg/kg were observed at station 04 (Fig. 3). At the

245   deep stations, particulate ^{232}Th ranged between 10 pg/kg and ~80 pg/kg, where lower

246   concentrations were observed at the ocean interior (St. 101 and 50) compared to the margin

247   (St. 32) (Fig. 3).

248

249   3.3 Dissolved ^{231}Pa$_{xs}$ and ^{230}Th$_{xs}$ concentrations

250   Measured concentrations of ^{231}Pa and ^{230}Th must be corrected for the presence of detrital

251   components due to the presence of U in lithogenic particles. The concentration of lithogenic U

252   is estimated from the measured concentrations of ^{232}Th, which is entirely of lithogenic origin

253   (Brewer et al., 1980). As U is assumed to be at secular equilibrium in lithogenic phases, the

254   unsupported ^{231}Pa and ^{230}Th (^{231}Pa$_{xs}$ and ^{230}Th$_{xs}$) produced solely by radioactive decay of

255   dissolved U-isotopes can be calculated:

256

257    $^{230}Th_{xs} = {}^{230}Th_m - {}^{232}Th_m \times \left(\frac{{}^{230}Th}{{}^{232}Th}\right)_{Litho} \times \frac{M230}{M232}$ (1)

258

259    $^{231}Pa_{xs} = {}^{231}Pa_m - {}^{232}Th_m \times \left(\frac{{}^{230}Th}{{}^{232}Th}\right)_{Litho} \times \left(\frac{{}^{235}U}{{}^{238}U}\right)_{Nat} \times \frac{\lambda_{230}}{\lambda_{238}} \times \frac{\lambda_{235}}{\lambda_{231}} \times \frac{M231}{M232}$ (2)

260

261   where the subscript m refers to measured concentrations of ^{231}Pa, ^{230}Th (fg/kg) and

262   ^{232}Th (pg/kg) in seawater and particles. The $\left(^{235}U/^{238}U\right)_{Nat}$ is the natural ^{235}U/^{238}U ratio of

263   1/137.88 (atom/atom) (Condon et al., 2010) and the $(^{230}Th/^{232}Th)_{Litho}$ was estimated from the

264   average activity ratio $[^{238}U/^{232}Th] = 0.6 \pm 0.3$. This range is relatively large compared to values

265   used previously for the Arctic Ocean ($[^{238}U/^{232}Th] = 0.6 \pm 0.1$, Moran et al., 2005b). It allows

266   covering the high value ($[^{238}U/^{232}Th] \approx 0.9$) deduced from the $^{230}Th/^{232}Th$ (= 4.75×10^{-6} mol/mol)

267   measured in the dirty ice, as well as the low ratio ($[^{238}U/^{232}Th] = 0.3$) inferred from the filtered

268   particles at station 04 to avoid "negative $^{231}Pa_{xs}$-values" in (see section 3.4). The secular

269   equilibrium in the lithogenic fraction of marine sediment is at has been questioned due to the

270   possible loss of ^{234}U (through ^{234}Th, its parent isotope), ^{230}Th and ^{231}Pa (through ^{231}Th, its

271   parent isotope) by α-recoil (Bourne et al., 2012). At present, it is unclear if this process is

272   sufficient to explain the discrepancy between the 2 estimates of the $[^{238}U/^{232}Th]$ activity ratio

273   presented here. Therefore, we conservatively consider the range $[^{238}U/^{232}Th] = 0.6 \pm 0.3$ as

274   possible and to propagate the resulting uncertainties. The same lithogenic corrections have

275   been made for the dissolved concentrations of ^{231}Pa and ^{230}Th at stations 50 and 125

276   measured by Valk et al., (2018).

277    $\lambda_{230}, \lambda_{231}, \lambda_{235}$ and λ_{238} are the decay constants for ^{230}Th ($\lambda_{230} = 9.16 \times 10^{-6}$ y^{-1}), ^{231}Pa

278   ($\lambda_{231} = 2.11 \times 10^{-5}$ y^{-1}), ^{235}U ($\lambda_{235} = 9.85 \times 10^{-10}$ y^{-1}) and ^{238}U ($\lambda_{238} = 1.55 \times 10^{-10}$ y^{-1}), respectively

279   (Cheng et al., 1998; Condon et al., 2010). *M230, M231* and *M232* are the atomic masses of

280   ^{230}Th (230.033 g/mol) ^{231}Pa (231.036 g/mol) and ^{232}Th (232.038 g/mol). The concentrations of

281   ^{231}Pa and ^{230}Th can be converted to radioactivity units (μBq/kg) by using the conversion factors

282   0.5724 and 1.3110, respectively. ^{232}Th concentrations can be converted to pmol/kg using the

283   atomic mass of ^{232}Th (232.038).

284   Higher lithogenic content was observed in particles and seawater collected at the

285   shelf, margin and in bottom waters of the deep basins. On average, the lithogenic contribution

286   ranged between 0.04 and 33 % for dissolved ^{231}Pa, between 2.3 and 72 % for particulate ^{231}Pa,

287   between 0.3 and 34 % for dissolved ^{230}Th and between 1.0 and 58 % for particulate ^{230}Th.

288   In the deep Arctic Basin, the observed dissolved concentrations of $^{231}Pa_{xs}$ and $^{230}Th_{xs}$

289   are increasing with depth until ~2000 m, followed by decreasing or invariant concentrations

290   approaching the seafloor. This depletion at depth was more pronounced at the Nansen Basin

291   stations (32, 40, 50) compared to the Makarov Basin station (101). The depletion of $^{230}Th_{xs}$ in

292   the Nansen Basin was greater compared to the decrease of dissolved $^{231}Pa_{xs}$ in waters below

293   2000 m depth (Fig. 2).

294   In the Makarov Basin, dissolved $^{231}Pa_{xs}$ ranged between 0.02 and 4.0 fg/kg and

295   concentrations of dissolved $^{230}Th_{xs}$ ranged between 0.9 and 27.9 fg/kg. In contrast, lower

296   concentrations of dissolved $^{231}Pa_{xs}$ (0.19 − 1.9 fg/kg) and $^{230}Th_{xs}$ (2.1 − 8.9 fg/kg) were

297   observed at the deep stations of the Eurasian Basin (Fig. 2).

298   In the Barents Sea, concentrations of dissolved $^{231}Pa_{xs}$ were lower in the polar waters

299   of stations 04 and 18 (0.1 − 0.2 fg/kg) compared to the inflowing Atlantic Water stations 153

300 and 161 (0.23 – 0.6 fg/kg), while the dissolved $^{231}Pa_{xs}$ in shallow waters (<500 m) over the

301 slope (St 32) and in the Nansen Basin (stations 40 and 50) ($^{231}Pa_{xs}$ = 0.20 – 0.4 fg/kg) are

302 intermediate between the Atlantic inflowing water (St. 153, 161) and close to Svalbard (St. 4).

303 The distribution of dissolved $^{230}Th_{xs}$ was similar for all four shelf stations (0.5 – 1.99

304 fg/kg) (Fig. 2) and generally lower compared to water at corresponding depth of the interior

305 basin (2.3 – 3.8 fg/kg) (Fig. 2).

306 At station 125, located in the Amundsen Basin, the water column distribution of

307 dissolved ^{231}Pa was similar compared to the stations located in the Nansen Basin, while

308 concentrations of dissolved ^{230}Th in the Nansen Basin (St. 32, 40, 50) were similar or higher

309 compared to the distribution of dissolved ^{230}Th from 500 m to 2000 m depth at station 125 (Fig.

310 2).

311

312 3.4 Particulate $^{231}Pa_{xs}$ and $^{230}Th_{xs}$ concentrations

313 The filtered particles from station 04 (Tab. ES2) and the dirty ice (Tab. ES3) were used to

314 determine the range of [$^{238}U/^{232}Th$] activity ratios of the lithogenic material. There was a high

315 abundance of lithogenic particles at station 04 (^{232}Th = 46 – 2400 pg/kg) and these particles

316 have low $^{231}Pa/^{232}Th$ ratios that must be supported by a [$^{238}U/^{232}Th$] activity ratio of ~ 0.3 (to

317 avoid negative values of $^{231}Pa_{xs}$), a value that we take as the lower limit of the [$^{238}U/^{232}Th$]

318 activity ratio of the lithogenic material. Ice rafted sediments embedded in sea ice (called "dirty

319 ice") are an important source of lithogenic particles in the Arctic Ocean (Pfirman and Thiede,

320 1987). As dirty ice is formed on the shelf, it may contain shelf sediments that have been

321 incorporated into the ice as anchor ice or by sediment resuspension. This means that the dirty

322 ice could contain some $^{230}Th_{xs}$ that has been scavenged over the shelf. Here, the $^{230}Th/^{232}Th$

323 ratio (= 4.75×10^{-6} mol/mol) of dirty ice is supported by a [$^{238}U/^{232}Th$] activity ratio of ~ 0.9, a

324 value in good agreement with the estimate of the average continental crust suggesting that

325 dirty ice is free of $^{230}Th_{xs}$. Therefore, we take 0.9 as the upper limit of the [$^{238}U/^{232}Th$] activity

326 ratio of the lithogenic material.

327 Concentrations of particulate $^{231}Pa_{xs}$ and $^{230}Th_{xs}$ in the Arctic Ocean generally display

328 an increasing trend with depth. Particulate concentrations of $^{231}Pa_{xs}$ ranged between 0.0004

329 and 0.08 fg/kg and particulate $^{230}Th_{xs}$ concentrations ranged between 0.001 and 5.6 fg/kg.

330 Elevated particulate $^{231}Pa_{xs}$ and $^{230}Th_{xs}$ concentrations were observed close to the seafloor at

331 stations 04, 153 and 161 and in deep waters of the Nansen and Makarov Basins (Fig. 3). Due

332 to the high abundance of particulate ^{232}Th at station 04 (^{232}Th = 46 – 2400 pg/kg), it was not

333 possible to estimate the unsupported particulate $^{231}Pa_{xs}$ concentrations for this station (see

334 above).

335   In the interior Nansen (Station 50), the distribution of particulate $^{231}Pa_{xs}$ and $^{230}Th_{xs}$
336   displayed an increase with depth until ~3000 m, followed by a decrease in particulate
337   concentrations approaching the seafloor. At station 32, concentrations of particulate $^{230}Th_{xs}$
338   ranged between 0.02 and 5.6 fg/kg, which was similar to concentrations observed at station
339   50 (0.28 – 5.9 fg/kg). In contrast, particulate $^{231}Pa_{xs}$ (>2000 m) was lower at the slope (0.05 –
340   0.08 fg/kg) compared to the interior (0.13 – 0.18 fg/kg) (Fig. 3).

341   The distribution of particulate $^{230}Th_{xs}$ observed at station 101 was very similar to the
342   slope and interior of the Nansen Basin, while, below 1500 m, the particulate $^{231}Pa_{xs}$
343   concentrations were lower in the Makarov Basin compared to the stations located in the
344   Nansen Basin (Fig. 3). As this manuscript was already submitted, the intercomparison work
345   revealed that the particulate ^{231}Pa concentrations at station 101 are ~ 50% lower than at the
346   nearby station of the USCGC Healy HLY1502 (GN01) cruise in 2015 (while particulate Th
347   isotopes are essentially similar at the 2 stations). Therefore, the interpretation of particulate Pa
348   data requires caution.

349   Before we can compare particulate $^{230}Th_{xs}$ and $^{231}Pa_{xs}$ in the water column with
350   measurements in the surface sediment, we must first evaluate if an age correction is required
351   for the sediment samples, as the sedimentation rate in the Arctic Ocean can be very low.
352   Sedimentation rate estimates in the Makarov Basin range from 0.4 to 4 cm/ky (e.g. Nowaczyk
353   et al., 2001). It corresponds at most to a mean age of 1.2 ky for the 1st cm of the sediment
354   core, so that it is not necessary to correct the $^{231}Pa_{xs}/^{230}Th_{xs}$ ratio for radioactive decay in the
355   sediment. The higher sedimentation rates encountered over the Barents Sea and slope make
356   age corrections negligible (Ivanova et al., 2002). We have determined the ^{238}U and ^{234}U content
357   of the 3 sediments (Tab. ES3). The [$^{234}U/^{238}U$] activity ratio of the 3 sediments is slightly below
358   equilibrium suggesting the absence of seawater derived U, in agreement other arctic
359   sediments (Hillaire-Marcel et al., 2017). Hence, we can estimate the [$^{231}Pa_{xs}/^{230}Th_{xs}$] activity
360   ratio more precisely than based on the [$^{238}U/^{232}Th$] range determined for the suspended
361   particles.

362   3.5 The Fractionation factor

363   The fractionation factor ($F_{Th/Pa}$) was calculated as follows:

364

365    $F_{Th/Pa} = (^{230}Th_{xs}/^{231}Pa_{xs})_p/(^{230}Th_{xs}/^{231}Pa_{xs})_d$ (3)

366

367   Fractionation factors obtained in this study ranged between 2.7 and 25.4 (Fig. 4).
368   They are comparable to values reported from other ocean basins (e.g. Hayes et al., 2015a;
369   Moran et al., 2002, 2001; Scholten et al., 2008). The distribution of $F_{Th/Pa}$ with depth was rather
370   constant (Fig. 4). Below 1000 m depth, fractionation factors were consistently lower at station

11

50 in the interior of the Nansen Basin (2.7 – 13.3) compared to the Nansen margin (3.7 – 22.3) and the Makarov Basin (7.2 – 25.4) (Fig. 4).

4 Discussion

4.1 $^{230}Th_{xs}$ and ^{232}Th scavenging in the Arctic Ocean

Early studies of $^{210}Pb_{xs}$ and $^{230}Th_{xs}$ in Arctic sediments highlighted that their inventory in the sediments exceeded the supply from the overlying water column near the slopes and shelves and were greater at the margins compared to the interior basins (Huh et al., 1997; Smith et al., 2003). This process, usually referred to as boundary scavenging was expected to be pronounced in the Arctic Ocean due to the high proportion of shelf areas with the associated high particle flux versus the low particle flux regions in the ice-covered interior basins (Bacon et al., 1989; Cochran et al., 1995; Edmonds et al., 2004; Scholten et al., 1995). Early studies estimated the Th scavenging rates using a simple 1D production-vertical scavenging model (Bacon et al., 1989; Edmonds, 1998; Scholten et al., 1995), but this view was later challenged to include the effect of lateral transport, the effect of deep water ventilation (Scholten et al., 1995) and boundary scavenging (Roy-Barman, 2009). Box-modelling using sedimentary and dissolved $^{230}Th_{xs}$ and $^{231}Pa_{xs}$ data suggests that ~90 % of the *in-situ* produced $^{230}Th_{xs}$ was removed within the Arctic Ocean by particle scavenging and that a large fraction of the scavenged $^{230}Th_{xs}$ was removed by boundary scavenging along the Arctic margins (Moran et al., 2005, Roy-Barman, 2009). The dataset presented here will be used to revisit our understanding of the scavenging processes in the Arctic Ocean. We start the discussion with ^{230}Th because it is highly particle reactive (relative to Pa) and currently used to study and identify variations in scavenging intensity (e.g. Roy-Barman, 2009; Hayes et al., 2015).

4.1.1. The Makarov Basin

When lateral transport can be neglected, the 1D reversible scavenging model predicts a linear increase of both dissolved $^{230}Th_{xs}$ ($^{230}Th_{xs-d}$) and particulate $^{230}Th_{xs}$ ($^{230}Th_{xs-p}$) concentrations with depth and consequently produces a constant $^{230}Th_{xs-p}/^{230}Th_{xs-d}$ ratio throughout the water column (Bacon and Anderson, 1982). Among all stations reported here, these conditions seem best fulfilled at station 101 in the Makarov Basin, particularly above 2000 m depth (Fig. 2 and 3). Station 101 is located in the Makarov Basin at high latitude isolated from continental margins. Therefore St. 101 can be used as a reference station to evaluate the effect of continental margins on the scavenging in the interior ocean. Neglecting horizontal transport,

403   the $^{230}Th_{xs-p}$ concentration is a function of the settling rate (S) of small particles and of the water

404   depth (h):

405

406    $$S = \frac{P_{230Th} \times h}{^{230}Th_{xs-p}}$$ (4)

407

408   where the P_{230Th} is the production rate of ^{230}Th in the water column (0.56 fg/kg/y). The settling

409   rate (S) of particles (> 0.8 μm) in the Makarov Basin ranged between 340 - 440 m/y, which is

410   consistent with earlier estimates in the central Arctic Ocean (e.g. Edmonds et al., 2004;

411   Scholten et al., 1995) and very close to new estimates e.g. S = 434 m/y (Rutgers Van Der

412   Loeff et al., 2018) However, it may represent an upper limit for the particle settling speed in the

413   central Arctic, because this calculation neglects the possible role of boundary scavenging

414   (Roy-Barman, 2009). The scavenging residence time of $^{230}Th_{xs}$ (~55 y) is much shorter than

415   the water ventilation residence time in the Makarov Basin (e.g. Scholten et al., 1995). Since

416   particle fluxes in the Makarov Basin are low and the water residence time is high, dissolved

417    $^{230}Th_{xs}$ concentrations have more time to build up by the decay of uranium and stay in solution

418   (Fig. 2). The particulate/total ratio of $^{230}Th_{xs}$ is relatively low (6-16%) and tends to increase with

419   depth at station 101 (Fig. 5).

420   Below 2000 m depth, dissolved $^{230}Th_{xs}$ displayed more invariant concentrations

421   followed by decreasing concentrations approaching the seafloor (Fig. 2). The ventilation of the

422   deep Arctic could contribute to produce such concave profiles (Scholten et al., 1995). However,

423   the ventilation age of the deep Makarov Basin is hundreds of years, which is much longer

424   compared to the ^{230}Th scavenging residence time (e.g. Rutgers van der Loeff et al., 2018).

425   These depleted concentrations of dissolved $^{230}Th_{xs}$ and ^{232}Th close to the seafloor were

426   accompanied with elevated concentrations of particulate $^{230}Th_{xs}$ and ^{232}Th (Fig. 3), suggesting

427   enhanced removal of dissolved $^{230}Th_{xs}$ close to the seafloor. No benthic nepheloid layer was

428   detected by transmission (Fig. ES4). However, even a slight increase in resuspended

429   sediments (not detectable by the transmissometer) may be sufficient to enhance scavenging

430   and removal of dissolved ^{230}Th close to the seafloor.

431   4.1.2. The Eurasian Basin

432   A sharp depletion of $^{230}Th_{xs}$ observed in deep waters (>2000 m) of the Nansen was recently

433   attributed to removal of $^{230}Th_{xs}$ related to release of dissolved iron from hydrothermal vents at

434   the Gakkel ridge (Valk et al., 2018). Therefore, the following discussion will mainly be divided

435   into water masses above and below 2000 m depth.

436

4.1.2.1 Waters above 2000 m

On the Barents shelf, the temperature and salinity at station 153 and 161 clearly indicate the inflow of saltier and warmer AW (Fig. ES2). As a consequence, the dissolved $^{230}Th_{xs}$ concentrations (Fig. 2) compare well to surface concentrations from the northern Atlantic Ocean (Hayes et al., 2015a). Close to the seafloor at station 153 and 161 elevated particulate $^{230}Th_{xs}$ and ^{232}Th concentrations were observed (Fig. ES2). The increased particulate fraction of $^{230}Th_{xs}$ at the bottom of the water column accompanied with reduced dissolved $^{230}Th_{xs}$ indicates bottom scavenging over the shelf (Fig. 2 and 3). The low beam transmission (300 – 450 m depth) reflects resuspension of bottom sediments resulting in enhanced scavenging (Fig. ES4). This probably happens due to the inflow of AW over the Barents Sea shelf which disrupts the sediments close to the seafloor (Lukashin and Shcherbinin, 2007).

At stations 04 and 18, the polar waters was less salty and colder compared to the Atlantic inflow, suggesting influence of ice melt and runoff close to the coast of Svalbard (Fig. 3). This was also reflected by the low beam transmission in the surface and bottom waters over the Barents shelf, indicating the presence of suspended particulate material (Fig. ES4). In addition, extremely high concentrations of particulate ^{232}Th (up to ~2400 pg/kg) and elevated concentrations of dissolved ^{232}Th (100 – 200 pg/kg) were observed at station 04 and 18, suggesting that the particulate material is dominated by lithogenic inputs and partial dissolution of these particles (Fig. 2). Nevertheless, the dissolved $^{230}Th_{xs}$ concentrations at stations 04 and 18 compare well with those of stations 153 and 161 suggesting that the water flow rate does not leave enough time for net scavenging to occur.

Station 32 and 40 are located within the FSBW, where the modified Atlantic inflow (~2.5°C) can be recognized between ~100 and 1000 m depth, followed by colder and less salty deep waters (Fig. ES2). Concentrations of dissolved $^{230}Th_{xs}$ in surface waters at station 32 and 40 (2.3 – 2.7 fg/kg) were within the range but on the high side of North Atlantic ($^{230}Th_{xs}$ = 0.76 – 3.4 fg/kg, Hayes et al., 2015) and Norwegian Sea ($^{230}Th_{xs}$ = 0.6 – 2.3 fg/kg, Moran et al., 1995) values.

At station 32 and 40, dissolved $^{230}Th_{xs}$ increases linearly with depth until ~1500 m and then becomes constant (Fig. 2). This departure from the equilibrium profile suggests the possibility of enhanced scavenging at the margin. By contrast, Station 50 (Valk et al., 2018) is located within the return flow of the FSBW (Fig. ES2 and ES3). Dissolved $^{230}Th_{xs}$ concentrations increase linearly down to 2000 m and they are higher than at station 32 and 40 indicating a lower scavenging rate. Surprisingly, the distribution of particulate $^{230}Th_{xs}$ was very similar at stations 32 and 50 (and also at station 101) (Fig. 3).

471   Elevated concentrations of particulate ^{232}Th at the margin (St. 32) compared to the

472   inner ocean (St. 50) are likely due to the advection of shelf waters (St. 4) transporting ^{232}Th

473   into the interior basin.

474   The dissolved ^{230}Th$_{xs}$ concentrations were considerably lower in the Amundsen basin

475   (station 125) compared to the Makarov basin (station 101) (Fig. 2), as shown previously

476   (Scholten et al., 1995; Valk et al., 2018). This reflects the large difference in water residence

477   times between the Makarov and Amundsen Basins (Schlosser et al., 1997), where the longer

478   water residence time in the Makarov Basin allows the concentrations of ^{230}Th$_{xs}$ to build up over

479   time by the decay of U, whereas waters from the Amundsen Basin were submitted to boundary

480   scavenging while flowing along the eastern Siberian margin.

481   Except the surface samples (<100 m), the dissolved ^{230}Th$_{xs}$ concentrations are

482   significantly lower in the Nansen and Amundsen Basins (St. 50, 40, 32 125) compared to the

483   Makarov Basin (St. 101). Within the Eurasian Basins (above 2000 m), a horizontal gradient of

484   dissolved ^{230}Th$_{xs}$ content between stations 125, 32, 40 and 50 was observed (Fig. 2). At station

485   50, dissolved ^{230}Th$_{xs}$ concentrations were highest, followed by intermediate concentrations at

486   the Nansen margin (St. 32, 40) and the lowest dissolved ^{230}Th$_{xs}$ were observed at station 125.

487   This suggests that ^{230}Th$_{xs}$ is scavenged along the boundaries as the dissolved ^{230}Th$_{xs}$ is

488   decreasing towards the margin. The water at station 125 has probably experienced more

489   scavenging on the Kara and Laptev shelf compared to the Barents shelf. Another possible

490   reason for the low ^{230}Th$_{xs}$ concentrations observed at 125 is scavenging onto particles carried

491   by the TPD (Trans Polar Drift) (Charette, pers. com.).

492

493   **Below 2000 m**

494   Below 2000 m, the ^{230}Th$_{xs}$ concentrations are relatively constant and identical within the

495   Eurasian Basin. The sharp decrease at station 50 is clearly due to hydrothermal scavenging

496   (Valk et al., 2018). In 2015, there was no sign of a strong hydrothermal activity in the beam

497   transmission data suggesting that the hydrothermal event was over at the time of sampling

498   and that the hydrothermal plume had faded away (Fig. ES4). The major part of the

499   hydrothermal plume in the basin is expected to be transported out of the Nansen Basin along

500   the Gakkel Ridge directly towards Fram Strait (Fig. ES3). Therefore, the distribution of

501   dissolved ^{230}Th$_{xs}$ at stations 32, 40 and 125 are not directly downstream of station 50 and their

502   ^{230}Th$_{xs}$ do not necessarily represent hydrothermal scavenging conditions. Valk et al., (2018)

503   identified hydrothermal plume water by their high dissolved Fe content. The dissolved Fe

504   content of the deep waters at station 32 are higher than at station 50: it does not correspond

505   to an hydrothermal source, but to sediment resuspension at the slope as a source of dissolved
506   Fe (Klunder et al., 2012, Rijkenberg et al., 2018).

507   An additional argument for deep enhanced scavenging comes from ^{232}Th. In general,
508   dissolved ^{232}Th concentrations increases with depth in the deep ocean (e.g. Moran et al., 2002,
509   Scholten et al., 2008, Okubo et al., 2013). In the present study, ^{232}Th decrease with depth, a
510   feature that was already observed in the Arctic (Edmonds et al., 2004), but remained
511   unexplained. The lack of increasing dissolved ^{232}Th concentrations towards the seafloor
512   suggests enhanced bottom scavenging. The lowest dissolved ^{232}Th in the deep basins occurs
513   at station 50 suggesting the involvement of scavenging by the hydrothermal plume. However,
514   low deep dissolved ^{232}Th is also found in the Makarov Basin, where scavenging by a
515   hydrothermal plume is not suspected. Note that the higher concentrations at station 32 do not
516   necessarily represent a lower scavenging rate because a high scavenging rate can be
517   balanced by a high input flux by particle resuspension/dissolution as suggested by the
518   relatively low beam transmission and high particulate ^{232}Th at this station.

519

520 **The particulate fraction**

521   Despite different dissolved ^{230}Th$_{xs}$ profiles at stations 32, 50 (Nansen Basin) and 101 (Makarov
522   Basin), the particulate ^{230}Th$_{xs}$ concentrations above 2500 m depth were similar at these
523   stations (Fig. 3). By contrast, particulate ^{232}Th concentrations were higher at station 32
524   compared to stations 50 and 101, highlighting the role of the continental margins in providing
525   high levels of particulate matter into the low productivity interior ocean.

526   The particulate fraction of ^{230}Th$_{xs}$ increases with depth at stations 32 and 50 from 1%
527   to 45% with a local maximum (20 %) around 200 m (Fig. 5). This subsurface maximum
528   particulate fraction can be related to the high ^{230}Th$_{xs}$ particulate fractions associated to the
529   bottom nepheloid layers on the shelf at station 153 and 04. Despite the high concentrations of
530   particulate ^{230}Th$_{xs}$ in the Makarov Basin, the ^{230}Th$_{xs}$ particulate fractions are higher at stations
531   32 and 50 because the dissolved ^{230}Th$_{xs}$ concentrations are much lower in the Nansen Basin
532   compared to the Makarov Basin. At station 32 and 101, the increased particulate fraction of
533   ^{230}Th$_{xs}$ at the bottom of the water column accompanied with reduced dissolved ^{230}Th$_{xs}$ indicates
534   bottom scavenging in deep waters of the open basin as it was already observed over the shelf
535   (Fig. 2 and 3). At station 50, the increased ^{230}Th$_{xs}$ particulate fraction of the bottom waters is
536   the relic of a hydrothermal plume induced scavenging event, possibly at a stage where the
537   steady state situation is being achieved again (Valk et al., 2018).

538

4.2 Modelling ^{230}Th scavenging in the Arctic Ocean

540 Several features listed in previous sections of this paper (increasing ^{230}Th$_{xs}$ particulate fraction

541 with depth; decreasing dissolved ^{230}Th$_{xs}$ content in the deepest waters of the ocean margin)

542 are not consistent with the 1D scavenging models that predict a linear increase of dissolved

543 and particulate ^{230}Th$_{xs}$ concentrations with depth and a constant ^{230}Th$_{xs}$ particulate fraction with

544 depth (e.g. Bacon and Anderson, 1982, Roy-Barman et al., 1996). They are not consistent with

545 the boundary scavenging model of Roy-Barman (2009) either, because this model predicts a

546 rather linear increase of dissolved ^{230}Th$_{xs}$ with depth at the margin and a constant ^{230}Th$_{xs}$

547 particulate fraction with depth. This is certainly due to an oversimplification of the particle

548 dynamics: particles were assumed to have a constant vertical flux and their transport between

549 the margin and the ocean interior was neglected. To overcome these assumptions, we propose

550 a boundary scavenging model where particles are introduced both at the ocean surface and

551 also throughout the water column at the margin (hypothesis 1) and where particles are

552 transported between the margin and the ocean interior (hypothesis 2). The input of particles at

553 all depths of the ocean margin can be viewed as a result of nepheloid layers on the shelf or on

554 the slope and/or to the chemical evolution of particles as they settle through the water column

555 (precipitation of Fe-Mn oxyhydroxides at depth for example). A key point is that the particles

556 introduced at depth are assumed to be free of ^{230}Th$_{xs}$ and ^{231}Pa$_{xs}$ when they are introduced in

557 the water column, so that the input of particles will not be associated with an input of ^{230}Th$_{xs.}$

558 and ^{231}Pa$_{xs}$ (hypothesis 3). This means that the particles are not merely resuspended local

559 bottom sediments, which are known to contain ^{230}Th$_{xs}$. Instead, we hypothesize that nepheloid

560 layers flow downward as turbidity currents along the slope with no or little mixing with

561 surrounding waters so that they may not scavenge ^{230}Th until they detach from the slope. Only

562 then, particles spread and scavenge ^{230}Th$_{xs}$ from the deep waters. This view differs from

563 Rutgers van der Loeff and Boudreau (1997), who assumed equilibration between seawater

564 and particles. Hypothesis (3) is required because a dissolved ^{230}Th$_{xs}$ depletion compared to

565 the equilibrium profile cannot be produced by resuspension of sediments that would already

566 be "equilibrated" with overlying seawater. Hypothesis (3) is crucial for creating a water column

567 ^{230}Th$_{xs}$ profile as observed in this study. Transport of particles between the margin and the

568 inner ocean (hypothesis 2) allows that most particles in the ice-covered central Arctic are

569 advected from the margins.

570

571 4.2.1. Transport of water

572 In this box model, the Arctic Ocean is divided into 2 boxes: the ocean margin and the ocean

573 interior (Fig. 6). The water volumes of the margin and of the ocean interior are V_m and V_i (m^3)

574 (Jakobsson, 2002). These 2 boxes exchange a total flux of water F (m^3/s). For simplicity, we

575 assume that the water flows horizontally between the boxes. Vertical mixing and ventilation of

576 water by inputs through Fram strait and Barents Sea are neglected. Hence, at any depth in the

577 water column the residence time of the water with respect to horizontal exchange is $\tau_m = V_m/F$

578 at the margin and $\tau_i = V_i/F$ at the ocean interior (Tab. 1). The time constant associated to water

579 transport are $k_m = 1/\tau_m$ and $k_i = 1/\tau_i$. The time constant associated with water exchange between

580 the ocean margin and the ocean interior are $k_m = 1/\tau_m$ for the ocean margin and $k_i = 1/\tau_i$ for the

581 ocean interior.

4.2.2. Particle transport

583 In this study, the concentration of particles was not measured. The particle concentration is

584 embedded in the dissolved-particulate partition coefficient K, introduced in the following

585 section. We scale the impact of particle concentration on the partition coefficient K with a

586 parameter m assumed to be proportional to the particulate concentration:

587

588 $$m = P(z)/P^m(0) \tag{5}$$

589 where P is the particle concentration (at the margin or in the ocean interior) and $P^m(0)$

590 is the particle concentration in the surface water of the ocean margin. Hence, $m^m = 1$ in the

591 surface water of the ocean margin and m is proportional to the particle concentration

592 elsewhere.

593 The conservation equations for m^m and m^i at the ocean margin and in the inner ocean

594 include particle production throughout the water column at the margin (hypothesis 1) and

595 particle transport between the margin and the inner ocean (hypothesis 2) and are given by:

596 $$\frac{dm^m}{dt} = -S^m \frac{dm^m}{dz} + k_m(m^i - m^m) + \mu \times m^m \tag{6}$$

597 $$\frac{dm^i}{dt} = -S^i \frac{dm^i}{dz} + k_i(m^m - m^i) \tag{7}$$

598 where S^m and S^i are the settling velocities of the particles at the margin and in the

599 inner ocean. They are both assumed to be constant with depth. We expect higher particle

600 settling rates at the margin compared to the interior due to increased production and the

601 associated particle flux (Anderson et al., 1983). μ is an arbitrary parameter aimed to produce

602 an exponential increase of the particle concentration in the deep waters. μ operates as if (1)

603 increasing turbulence towards the seafloor and increases the particle concentration by

604 formation of nepheloids and/or (2) a diffusive flux of dissolved Manganese (Mn) from the

605 sediment which allows precipitation of Mn oxides (that scavenges Pa and Th) towards the sea
606 floor. Assuming a steady state, we obtain:

607
$$\frac{dm^m}{dz} = \frac{k_m}{S^m}\left(m^i - m^m\right) + \frac{\mu}{S^m} \times m^m \tag{8}$$

608
$$\frac{dm^i}{dz} = \frac{k_i}{S^i}\left(m^m - m^i\right) \tag{9}$$

609 Bulk dissolution of particles was not considered. The observed increasing particulate [230]Th
610 fraction with depth points to an addition of particles with depth rather than a significant
611 dissolution with depth, which would induce a concave shaped [230]Th profile (Roy-Barman et al.,
612 1996). Moreover, there is no direct constraint on the particle dissolution in the present study.

613 4.2.3. Transport of [230]Th$_{xs}$ and [231]Pa$_{xs}$

614 In each box, [230]Th and [231]Pa$_{xs}$ are produced by *in-situ* decay of U at a constant rate *P*. The
615 produced [230]Th and [231]Pa$_{xs}$ are then transported towards the seafloor by reversible scavenging
616 onto sinking particles and transported horizontally by the flow of water (Fig. 6). Considering
617 the long half-life of [230]Th (75 000 y) and [231]Pa (32 700 y), the radioactive decay of the two
618 isotopes was neglected. Dissolved and particulate concentrations are noted as C_d^m and C_p^m for
619 the margin and C_d^i and C_p^i for the ocean interior. The conservation equation of total [230]Th is
620 given by:

621 The ocean margin:

622
$$\frac{d\left(C_d^m + C_p^m\right)}{dt} = -S^m \frac{dC_p^m}{dz} + k_m\left(\left[C_d^i + C_p^i\right] - \left[C_d^m + C_p^m\right]\right) + P_{230} \tag{10}$$

623 The ocean interior:

624
$$\frac{d\left(C_d^i + C_p^i\right)}{dt} = -S^i \frac{dC_p^i}{dz} + k_i\left(\left[C_d^m + C_p^m\right] - \left[C_d^i + C_p^i\right]\right) + P_{230} \tag{11}$$

625 At the margin (equation 10), the only source term is the *in-situ* production because
626 the particles introduced in the water column of the margin do not contain [230]Th$_{xs}$ (hypothesis
627 3). The relationship between C_d and C_p is obtained by assuming a reversible equilibrium
628 between dissolved and particulate Th:

629
$$C_p^i = K \times m^i \times C_d^i \tag{12}$$

630
$$C_p^m = K \times m^m \times C_d^m \tag{13}$$

where K is the equilibrium coefficient of Th or Pa between the particulate fraction (mass of radionuclide carried by particles per L of seawater) and the dissolved fraction (mass of radionuclide in solution per L of seawater) (K = concentration in particles/concentration in the dissolved phase). K is assumed to be constant with depth and particle concentration. Assuming a steady state, we obtain:

$$\frac{d(m^m C_d^m)}{dz} = \frac{1}{S^m}\left\{ k_m \left((1 + K \times m^i)C_d^i - (1 + K \times m^m)C_d^m \right) + P_{230} \right\} \tag{14}$$

$$\frac{d(m^i C_d^i)}{dz} = \frac{1}{S^i}\left\{ k_i \left((1 + K \times m^m)C_d^m - (1 + K \times m^i)C_d^i \right) + P_{230} \right\} \tag{15}$$

Equations 10, 11, 14 and 15 are solved numerically. We use circulation parameters already obtained for modelling the boundary scavenging in the Arctic Ocean (Roy-Barman, 2009). The water residence time with respect to horizontal exchange is 10 y for the ocean margin and 50 y for the ocean interior (Tab. 1). All the other parameter are adjusted by trial and error in order to obtain a reasonable agreement (Fig. 7) with the dissolved and particulate profiles of station 32 (Nansen margin) and station 50 (Nansen interior, above 2000 m to avoid the hydrothermal scavenging that is not represented in the model). Qualitatively equivalent results were obtained for station 32 and station 101 (not shown). The boundary conditions for the particle concentration are $m^m(0) = 1$ (by definition of m) and $m^i(0) = 1.5$ to obtain a reasonable fit between the model and the ^{230}Th profile (see discussion below). This implies that there is an input of particles in the surface waters at the margin and in the interior ocean. We use $\mu = 0.5$ y^{-1}. As the particle settling speed at the margin is set a 600 m/y, it corresponds to an increase of the particle concentration at the margin of a factor 2.71 every 1200 m of depth. By default, we choose the same value for K (= 0.11), at the margin and in the inner ocean. If we want to reproduce the similar vertical ^{230}Th$_p$ gradients observed at the margin and in the inner ocean (Fig. 3), the settling velocity of the particles must be higher at the margin (600 m/y) compared to the ocean interior (340 m/y. Indeed, if $\frac{dC_p^m}{dz} \approx \frac{dC_p^i}{dz}$, equations 14 and 15 can be combined to yield:

$$\frac{S^i}{S^m} \approx \frac{P_{230} - k_i\left(C_{d+p}^i - C_{d+p}^m\right)}{P_{230} + k_m\left(C_{d+p}^i - C_{d+p}^m\right)} \tag{16}$$

As $C_{d+p}^i - C_{d+p}^m > 0$, it follows that $S^i < S^m$

In other words, $S^i < S^m$ because at the margin, an excess of ^{230}Th advected from the inner ocean must be removed by settling particles with the same vertical ^{230}Th$_p$ gradient as in the inner ocean. Conversely, in the inner ocean, less ^{230}Th must be removed by settling

20

661 particles with the same vertical $^{230}Th_p$ gradient as at the margin. Note that $S^i = S^m$, only if $k_i =$

662 $k_m = 0$. This corresponds to the 1D reversible scavenging model that would not account for the

663 increasing ^{230}Th particulate fraction with depth and for the non-linear dissolved ^{230}Th profiles.

664 Given the simplicity of the model, we do not expect a full agreement with the data

665 despite some tuning of the parameters. For example, the hydrothermal scavenging of $^{230}Th_{xs}$

666 below 2000 m depth, possibly occurring at station 50 is not represented in the model.

667 Nevertheless, we believe that the model captures some effects of particle accumulation and

668 scavenging at depth. This is in line with 3D modelling results showing that dissolved Th and

669 Pa profiles in the Atlantic Ocean are better simulated when a parametrization of boundary and

670 bottom scavenging is introduced (Rempfer et al., 2017).

671 As observed in the data, the modelled dissolved $^{230}Th_{xs}$ concentration profiles

672 increase with depth followed by a decrease in concentration approaching the seafloor (Fig. 7).

673 The model also captures the linear increase of the particulate $^{230}Th_{xs}$ concentrations with depth,

674 as observed in the data (Fig. 7). Despite the reversible scavenging equilibrium hypothesis,

675 dissolved and particulate $^{230}Th_{xs}$ are not proportional because the mass of particles "*m*"

676 increases with depth (eq. 1). Therefore, the linear particulate $^{230}Th_{xs}$ profiles result from the

677 gross linear increase of the $^{230}Th_{xs}$ *in-situ* production with depth (it is not perfectly linear due to

678 lateral transport). Despite this linear increase of the particulate $^{230}Th_{xs}$, the dissolved $^{230}Th_{xs}$

679 concentrations can decrease with depth due to the increased particulate scavenging. As a

680 consequence of the dissolved and particulate profile shapes, the particulate/total fraction of

681 $^{230}Th_{xs}$ increases with depth as observed in the data (Fig. 5 and 7).

682 The measured particulate $^{230}Th_{xs}$ concentrations are relatively similar at stations 32,

683 50 and 101 (Fig. 3). This is surprising and probably circumstantial: the high particle mass

684 equilibrating with a low dissolved $^{230}Th_{xs}$ content at the margin balances the lower mass of

685 particles equilibrating with a higher dissolved $^{230}Th_{xs}$ concentration at the interior ocean. A

686 direct consequence of these similar particulate $^{230}Th_{xs}$ profiles is that the vertical flux of $^{230}Th_{xs}$

687 is increased at the margin where the particle settling velocity is higher compared to the ocean

688 interior. Hence, boundary scavenging occurs.

689

690 4.3 $^{231}Pa_{xs}$ profiles: scavenging versus circulation

691 $^{231}Pa_{xs}$ is less particle reactive compared to $^{230}Th_{xs}$, as indicated by the lower $^{231}Pa_{xs}$ particulate

692 fraction compared to the $^{230}Th_{xs}$ particulate fraction (Fig. 5). As a consequence, $^{231}Pa_{xs}$ profiles

693 generally deviate more strongly from the linear increase expected from reversible scavenging

694 due to a significant transport by advection (e.g. Hayes et al., 2015; Gdaniec et al., 2017). In

695 the Arctic, Moran et al. (2005) estimated that 39 % of the $^{231}Pa_{xs}$ produced in the Arctic Ocean

696 is expected to be exported to the Atlantic Ocean through the Fram Strait. However, in the

21

697   Makarov Basin, ventilation cannot account for the non-linear ^{231}Pa profile, as the residence

698   time of the deep water is several hundreds of years (e.g. Rutgers van der Loeff et al., 2018).

699   Therefore, this non-linear profile may be related to scavenging along the basin boundaries

700   (Roy-Barman, 2009).

701   On the Barents Shelf (St. 153 and 161), representing the inflow of unmodified Atlantic

702   waters, the dissolved ^{231}Pa$_{xs}$ is in the same range as the concentrations (^{231}Pa$_{xs}$ = 0.33 – 0.68

703   fg/kg) measured in the northeastern Atlantic (Hayes et al., 2015). At stations 04 and 18, the

704   dissolved ^{231}Pa$_{xs}$ (0.19 – 0.36 fg/kg) becomes slightly lower, possibly reflecting scavenging of

705   ^{231}Pa$_{xs}$ on the Barents Self (Fig. 2). Pa scavenging over the Barents Self is not surprising

706   because the area is known for its diatom blooms (Wassmann et al., 1990). The dissolved

707   ^{231}Pa$_{xs}$ in shallow waters (<500 m) over the slope (St. 32) and the Nansen Basin (stations 40

708   and 50) (^{231}Pa$_{xs}$ = 0.20 – 0.4 fg/kg) are intermediate between the Atlantic inflowing water

709   (stations 153 and 161) and close to Svalbard (St. 4).

710   As for the ^{230}Th$_{xs}$ (and ^{232}Th) in bottom waters of station 153 and 161, depleted

711   concentrations of dissolved ^{231}Pa$_{xs}$ were accompanied with elevated particulate ^{231}Pa$_{xs}$

712   concentrations (Fig. 2 and 3), indicating removal of ^{231}Pa$_{xs}$ at the Barents shelf, close to the

713   seafloor. The particulate fraction of ^{231}Pa$_{xs}$ in deep waters of the interior Nansen was very small

714   (0.2-0.9 %) compared to ^{230}Th$_{xs}$ (25-48 %), which is expected due to the overall lower particle

715   reactivity of ^{231}Pa (compared to ^{230}Th).

716   Extremely low dissolved ^{231}Pa$_{xs}$ concentrations (0.02 ± 0.005 fg/kg) were observed in

717   surface waters (10 – 100 m) of station 101 (Fig. 2). As the high ^{232}Th content of these waters

718   was attributed to advection by the transpolar drift (e.g. Rutgers van der Loeff et al., 2018), it is

719   likely that these waters were completely depleted of their ^{231}Pa over the shelf and that during

720   their transit to station 101 reversible scavenging has acted to build up a linear equilibrium

721   profile. The sea-ice cover has prevented this equilibrium profile (>100 m) from re-

722   homogenization by wind-induced mixing.

723   In the deep basins, deep/bottom scavenging also occurs, as suggested by the

724   elevated particulate ^{231}Pa$_{xs}$ concentrations below 2000 m depth observed at station 32 and 50

725   that indicate removal of ^{231}Pa$_{xs}$ in deep waters of the Nansen Basin (Fig. 3). However, in

726   contrast to ^{230}Th$_{xs}$, higher ^{231}Pa$_{xs}$ particulate fractions were observed at station 50 relative to

727   station 32 (Fig. 5), suggesting the presence at station 50 of hydrothermal particles which are

728   known to have a high affinity for Pa.

729   Unlike dissolved ^{230}Th$_{xs}$ profiles, the dissolved ^{231}Pa$_{xs}$ profiles in the Nansen and

730   Amundsen Basin have similar shapes probably due to the much longer scavenging residence

731   time of Pa relative to Th. By contrast, ^{231}Pa$_{xs}$ concentrations are higher in the intermediate/deep

732   Makarov Basin (St. 101) than in the Eurasian Basin due to the long term isolation of these 2

733   basins by the Lomonosov ridge (Fig. 2). Interestingly, there are two distinct correlations

734   between dissolved silica (DSi) and dissolved $^{231}Pa_{xs}$ in the deep waters of the Nansen and the

735   Makarov Basins (Fig. 8). These positive correlations are likely due to the high affinity of ^{231}Pa

736   for biogenic silica (BSi) (e.g. Chase et al., 2002). We propose that ^{231}Pa is scavenged by BSi

737   formed in surface waters. As these particles settle through the water column, BSi dissolves

738   and releases ^{231}Pa into solution again. The steeper slope of the dissolved $^{231}Pa_{xs}$ versus DSi

739   correlation in the Makarov Basin compared to the Nansen Basin is likely due to accumulation

740   of *in-situ* produced ^{231}Pa (in addition to the BSi dissolution effect) during the longer aging of

741   the deep Makarov/Canadian waters.

742

743   4.4. Applying the boundary scavenging model to Pa

744   The boundary scavenging model developed for ^{230}Th is now applied to ^{231}Pa with the

745   appropriate changes (Tab. 1). The production rate is changed (0.025 fg/kg/y) and the

746   dissolved-particulate partition coefficient is divided by 12 because we have estimated that

747    $F_{Th/Pa}$ ~ 12 (Fig. 4). Several similarities and differences arise between the model and measured

748   data.

749   The model reproduces the non-linear shape of the dissolved $^{231}Pa_{xs}$ profiles

750   (particularly at St. 50) and the relatively linear particulate $^{231}Pa_{xs}$ profiles of station 32 and 50.

751   However, the modelled dissolved $^{231}Pa_{xs}$ concentrations are overestimated by a factor 2 to 4

752   (Fig. 7). Modelled particulate $^{231}Pa_{xs}$ concentrations at the margin are also overestimated. The

753   reason for the overestimated dissolved $^{231}Pa_{xs}$ concentrations is probably a mix of previously

754   discussed processes and because of the possible underestimation of the particulate Pa

755   concentration revealed by intercomparison work at station 101 (higher particulate Pa

756   concentration would result in a higher removal rate by scavenging on setting particles).

757   Scavenging of $^{231}Pa_{xs}$ by hydrothermal plumes can severely deplete the concentrations of

758    $^{231}Pa_{xs}$ in the deep Arctic Ocean (Valk et al., 2018). Export of ^{231}Pa through advection has been

759   proposed to have a significant importance in several studies (e.g. Hoffmann et al., 2013; Moran

760   et al., 2005). The dissolved ^{231}Pa concentrations of the deep inflow through the Fram Strait

761   Branch (^{231}Pa ~1 –1.5 fg/kg) agrees well with the value (^{231}Pa = 1.5 fg/kg) used in Moran et al.

762   (2005). The ^{231}Pa concentrations reported here for the return in the Nansen Basin at station

763   50 (^{231}Pa ~ 1 – 1.5 fg/kg) is close to the Fram Strait Branch. By contrast, in the deep Makarov

764   Basin, above the sill on the Lomonosov ridge is (^{231}Pa ~1.5 – 3.0 fg/kg) consistent with Moran

765   et al (2005) estimates. This ^{231}Pa gradient between the inflow and outflow supports a net export

766   of ^{231}Pa into the Atlantic.

767   Finally, boundary scavenging along the slopes of the Eurasian Basin can reduce the

768   dissolved ^{231}Pa in the deep Arctic Ocean. Probably, $^{231}Pa/^{230}Th$ ratios of the suspended

769   particles of the Nansen Basin were below the $^{231}Pa/^{230}Th$ production ratio, but top-core

23

770 sediments of the Nansen margin and slope have high $^{231}Pa/^{230}Th$-ratios, suggesting that the
771 Nansen margin is in fact a large sink for ^{231}Pa in the Arctic Ocean.

772 Roy-Barman (2009) proposed a balanced Arctic budget of ^{231}Pa between the inner
773 ocean and the margin without export of ^{231}Pa through the Fram Strait. However, it was based
774 on very low $F_{Th/Pa}$ values (~ 3-10) compared to the values reported in the present work.

4.4 Factors controlling Pa-Th fractionation

4.4.1 The Th-Pa fractionation factor

777 $^{231}Pa_{xs}$ is generally less particle reactive than $^{230}Th_{xs}$, which results in $^{231}Pa_{xs}$ profiles that
778 deviate more strongly from the linear increase expected from reversible scavenging due to
779 transport by advection (e.g. Chase et al., 2002; Hayes et al., 2015; Gdaniec et al., 2017). The
780 particulate content of $^{231}Pa_{xs}$ relative to the total $^{231}Pa_{xs}$ concentrations was in the order of 0.6
781 – 1 % in the deep stations (<2000 m) and up to 15% on the shelf, while particulate/total ratios
782 for $^{230}Th_{xs}$ ranged between 6 % and 17 % in the deep stations and up to 80% on the shelf (Fig.
783 5). This reflects the preferential scavenging of $^{230}Th_{xs}$ relative to $^{231}Pa_{xs}$, As a consequence,
784 the $F_{Th/Pa}$ in the open ocean is typically around 20 (e.g. Hayes et al., 2015b), mostly when
785 carbonate, organic and lithogenic particles dominates. Notable exceptions are environments
786 where particulate matter is dominated by diatoms ($F_{Th/Pa}$ < 5, e.g. Scholten et al., 2008;
787 Venchiarutti et al., 2011a; Venchiarutti et al., 2011b) or Mn-Fe (oxy)hydroxides, such as in
788 hydrothermal plumes ($F_{Th/Pa}$ = 6 ± 3 for MnO_2 and $F_{Th/Pa}$ = 11 ± 6 for $Fe(OH)_3$, Hayes et al.,
789 2015; Pavia et al., 2018). As a consequence of these different drivers, 2 types of $F_{Th/Pa}$ depth
790 profiles are generally observed:

791 1) In the North Atlantic $F_{Th/Pa}$ decreases with depth because the particulate matter
792 composition evolves from lithogenic/carbonated in the surface water to strongly affected by
793 Fe-Mn oxides due to hydrothermal particles above and around the Mid-Atlantic Ridge or to
794 oxidation/precipitation of Fe-Mn released in the oxygen minimum zone off the Mauritanian
795 coast.

796 2) In areas dominated by diatom production, $F_{Th/Pa}$ tends to increase with depth as a
797 consequence of the biogenic silica dissolution (Scholten et al., 2008; Venchiarutti et al., 2011),
798 because opal tends to dissolve during the settling through the water column (Nelson et al.,
799 1995). In the Arctic, this view is supported by the strong correlation observed between
800 dissolved ^{231}Pa and dissolved Si of the deep Makarov and Nansen Basins (Fig 8).

801 The $F_{Th/Pa}$ profiles that we obtained on the Nansen margin (St. 32, 153 and 161) and
802 in the Makarov Basin (St. 101) show a clear increase with depth (from $F_{Th/Pa}$ ≈ 2-5 in the shallow
803 waters to $F_{Th/Pa}$ ≈ 20 in the deep waters) suggesting surface particles dominated by diatoms
804 and deeper particles with an increasing influence of lithogenic particles resuspended and
805 advected from the margin. At station 50, the limited increase of $F_{Th/Pa}$ below 2000 m ($F_{Th/Pa}$ ≈

806   10) supports that particles at this station still include some particles derived from the
807   hydrothermal activity, even if at the time of sampling most of the plume itself had left the Gakkel
808   ridge and cannot be clearly detected with beam transmission data (Valk et al., 2018).
809

810   4.4.2 Large scale Pa-Th fractionation

811   Early studies of Pa-Th in the Arctic Ocean have emphasized that despite of the large shelf
812   areas, the large Pa-Th fractionation observed in the Pacific Ocean sediments between the
813   ocean margin ($[^{231}Pa_{xs}/^{230}Th_{xs}] \approx 3$ * production ratio) and the ocean interior ($[^{231}Pa_{xs}/^{230}Th_{xs}] \approx$
814   0.3 * production ratio) was not present in Arctic Ocean sediments. Instead, most Arctic
815   sediments have $[^{231}Pa_{xs}/^{230}Th_{xs}]$ activity ratios significantly lower than the production ratio
816   (Edmonds et al., 2004; Moran et al., 2005). Recently, a few sediment samples collected on the
817   Siberian shelf margins were reported to have $^{231}Pa_{xs}/^{230}Th_{xs}$ ratios that slightly exceed the
818   production ratio (Luo and Lippold, 2015). Moreover, Hoffmann et al. (2013) observed
819   decreasing Arctic sedimentary $^{231}Pa/^{230}Th$ ratios with water depth, over the last 30 kyr. This
820   general deficit in $^{231}Pa_{xs}$ was attributed to the export of a significant fraction of the Arctic $^{231}Pa_{xs}$
821   into the Atlantic Ocean through the Fram Strait and to the hypothetical possibility that some of
822   the $^{231}Pa_{xs}$ was lost by boundary scavenging in a location not identified at that time.
823   The data obtained in this work on the suspended particles of the Nansen margin (St.
824   32, 158 and 161) show particulate $[^{231}Pa_{xs}/^{230}Th_{xs}]$ activity ratios below the production ratio
825   except in the surface waters, but the calculation of the particulate $^{231}Pa_{xs}$ is affected by large
826   uncertainties (Tab. ES2). However, Top-core sediments from the Nansen margin (St. 161 and
827   32) have distinctly high $[^{231}Pa_{xs}/^{230}Th_{xs}]$ activity ratios: $[^{231}Pa_{xs}/^{230}Th_{xs}]$ = 0.40 at station 161 and
828   0.18 at station 32 (Tab S3). Hence, the $[^{231}Pa_{xs}/^{230}Th_{xs}]$ activity ratios of these two surface
829   sediment samples are much higher than the corresponding ratio in the suspended particles.
830   These ratios at station 161 and 32 are well above the values reported by Moran et al. (2005).
831   So boundary scavenging along the Nansen margin could contribute to the ^{231}Pa depletion in
832   the Arctic Ocean. Scavenging by the hydrothermal plume turns out to be an alternative sink.
833   Moreover, the discrepancies between the sediment and particulate $^{231}Pa/^{230}Th$ ratios
834   might be related to the different timescales of these data records. Still, particulate samples in
835   the deep part of the station 50 have $^{231}Pa_{xs}/^{230}Th_{xs}$ ratios below the production ratio despite the
836   relatively low $F_{Th/Pa}$ (Tab. ES2). Whether these particles are still dominated by hydrothermal
837   particles or not remains ambiguous (Valk et al., 2018).

5 Conclusions

The distribution of $^{231}Pa_{xs}$ and $^{230}Th_{xs}$ in the Arctic Ocean deviates from the linear increase expected from reversible scavenging in absence of lateral advection. While the role of hydrothermal scavenging of ^{230}Th recently has been highlighted in the Nansen Basin (Valk et al., 2018), we show here that boundary scavenging also removes significant amounts of ^{230}Th at the Nansen margin.

Scavenging on particles derived from hydrothermal activity is associated with a relatively low $F_{Th/Pa}$ fractionation factor ($\approx$10), while higher $F_{Th/Pa}$ ($\approx$20) were observed for deep and bottom waters both of the Eurasian and Makarov Basin.

The modified boundary scavenging model developed here for the Nansen Basin, successfully modeled the increasing $^{230}Th_{xs}$ particulate fraction with depth and the decrease of dissolved Pa-Th contents approaching the seafloor observed on various margins. Modeled dissolved ^{231}Pa distributions were largely overestimated. These results suggest that advection of dissolved ^{231}Pa out the Atlantic is an important sink for the Arctic ^{231}Pa budget. However, the high sedimentary $^{231}Pa_{xs}/^{230}Th_{xs}$ ratios observed at the Barents Sea shelf and Nansen margin indicate that the Arctic margins could indeed act as a major sink for the missing Arctic ^{231}Pa. More data focused on shelves and slopes of the Arctic Ocean are required to better constrain this effect and the chemical nature of the particles and their physical mode of resuspension have to be addressed more precisely.

6 Acknowledgements

References

Aagaard, K., Britain, G., Aagaard, K., Carmack, E., 1981. On the halocline of the Arctic Ocean. Deep. Res. 28, 529–545.

Anderson, R.F., Bacon, M.P., Brewer, P.G., 1983. Removal of 230Th and 231Pa at Ocean Margins. Earth Planet. Sci. Lett. 66, 73–90. https://doi.org/10.1016/0012-821X(83)90127-9

871   Bacon, M.P., Anderson, R.F., 1982. Distribution of Thorium isotopes between dissolved and
872   particulate forms in the deep sea. J. Geophys. Res. 87, 2045–2056.
873   https://doi.org/10.1029/JC087iC03p02045

874   Bacon, M.P., Huh, C.A., Moore, R.M., 1989. Vertical profiles of some natural radionuclides
875   over the Alpha Ridge, Arctic Ocean. Earth Planet. Sci. Lett. 95, 15–22.
876   https://doi.org/10.1016/0012-821X(89)90164-7

877   Björk, G., Anderson, L.G., Jakobsson, M., Antony, D., Eriksson, P.B., Hell, B., Hjalmarsson,
878   S., Janzen, T., Jutterstr, S., Marcussen, C., Olsson, K.A., Rudels, B., Linders, J.,
879   Ludvig, L., Sølvsten, M., Selle, E., 2010. Deep-Sea Research I Flow of Canadian basin
880   deep water in the Western Eurasian Basin of the Arctic Ocean 57, 577–586.
881   https://doi.org/10.1016/j.dsr.2010.01.006

882   Björk, G., Jakobsson, M., Rudels, B., Swift, J.H., Anderson, L., Darby, D.A., Backman, J.,
883   Coakley, B., Winsor, P., Polyak, L., Edwards, M., 2007. Bathymetry and deep-water
884   exchange across the central Lomonosov Ridge at 88-89°N. Deep. Res. Part I
885   Oceanogr. Res. Pap. 54, 1197–1208. https://doi.org/10.1016/j.dsr.2007.05.010

886   Chase, Z., Anderson, R.F., Fleisher, M.Q., Kubik, P.W., 2002. The influence of particle
887   composition and particle flux on scavenging of Th, Pa and Be in the ocean. Earth
888   Planet. Sci. Lett. 204, 215–229. https://doi.org/10.1016/S0012-821X(02)00984-6

889   Cheng, H., Edwards, R.L., Murrell, M.T., Benjamin, T.M., 1998. Uranium-thorium-
890   protactinium dating systematics. Geochim. Cosmochim. Acta 62, 3437–3452.
891   https://doi.org/http://dx.doi.org/10.1016/S0016-7037(98)00255-5

892   Cochran, J.K., Hirschberg, D.J., Livingston, H.D., Buesseler, K.O., Key, R.M., 1995. Natural
893   and anthropogenic radionuclide distributions in the Nansen Basin, Artic Ocean:
894   Scavenging rates and circulation timescales. Deep. Res. Part II 42, 1495–1517.
895   https://doi.org/10.1016/0967-0645(95)00051-8

896   Condon, D.J., McLean, N., Noble, S.R., Bowring, S.A., 2010. Isotopic composition
897   (238U/235U) of some commonly used uranium reference materials. Geochim.
898   Cosmochim. Acta 74, 7127–7143. https://doi.org/10.1016/j.gca.2010.09.019

899   Edmonds, H.N., 1998. Protactinium-231 and Thorium-230 Abundances and High Scavenging
900   Rates in the Western Arctic Ocean. Science (80-.). 280, 405–407.
901   https://doi.org/10.1126/science.280.5362.405

902   Edmonds, H.N., Moran, S.B., Cheng, H., Edwards, R.L., 2004. 230Th and 231Pa in the
903   Arctic Ocean: Implications for particle fluxes and basin-scale Th/Pa fractionation. Earth
904   Planet. Sci. Lett. 227, 155–167. https://doi.org/10.1016/j.epsl.2004.08.008

905   Gdaniec, S., Roy-Barman, M., Foliot, L., Thil, F., Dapoigny, A., Burckel, P., Garcia-Orellana,
906   J., Masqué, P., Mörth, C.-M., Andersson, P.S., 2017. Thorium and protactinium isotopes
907   as tracers of marine particle fluxes and deep water circulation in the Mediterranean Sea.
908   Mar. Chem. 199, 12–23. https://doi.org/10.1016/j.marchem.2017.12.002

909   Guihou, A., Pichat, S., Nave, S., Govin, A., Labeyrie, L., Michel, E., Waelbroeck, C., 2010.

Late slowdown of the Atlantic Meridional Overturning Circulation during the Last Glacial Inception: New constraints from sedimentary (231Pa/230Th). Earth Planet. Sci. Lett. 289, 520–529. https://doi.org/10.1016/j.epsl.2009.11.045

Hayes, C.T., Anderson, R.F., Fleisher, M.Q., Huang, K.F., Robinson, L.F., Lu, Y., Cheng, H., Edwards, R.L., Moran, S.B., 2015a. [230]Th and [231]Pa on GEOTRACES GA03, the U.S. GEOTRACES North Atlantic transect, and implications for modern and paleoceanographic chemical fluxes. Deep. Res. Part II Top. Stud. Oceanogr. 116, 29–41. https://doi.org/10.1016/j.dsr2.2014.07.007

Hayes, C.T., Anderson, R.F., Fleisher, M.Q., Vivancos, S.M., Lam, P.J., Ohnemus, D.C., Huang, K.F., Robinson, L.F., Lu, Y., Cheng, H., Edwards, R.L., Moran, S.B., 2015b. Intensity of Th and Pa scavenging partitioned by particle chemistry in the North Atlantic Ocean. Mar. Chem. 170, 49–60. https://doi.org/10.1016/j.marchem.2015.01.006

Hillaire-Marcel, C., McManus, J., Ghaleb, B., Vernal, A. de, Maccali, J., Cuny, K., Jacobel, A., C. Le Duc, 2017. A New Chronology of Late Quaternary Sequences From the Central Arctic Ocean Based on '"Extinction Ages'" of Their Excesses in 231Pa and 230Th 4573–4585. https://doi.org/10.1002/2017GC007050

Hoffmann, S.S., McManus, J.F., Curry, W.B., Susan Brown-Leger, L., 2013. Persistent export of 231 Pa from the deep central Arctic Ocean over the past 35,000 years. Nature 497, 603–606. https://doi.org/10.1038/nature12145

Huh, C.A., Pisias, N.G., Kelley, J.M., Maiti, T.C., Grantz, A., 1997. Natural radionuclides and plutonium in sediments from the western Arctic Ocean: Sedimentation rates and pathways of radionuclides. Deep. Res. Part II Top. Stud. Oceanogr. 44, 1725–1743. https://doi.org/10.1016/S0967-0645(97)00040-4

Ivanova, E. V, Murdmaa, I.O., Duplessy, J., Paterne, M., 2002. Late Weichselian to Holocene paleoenvironments in the Barents Sea. Glob. Planet. Change 34, 209–218.

Jakobsson, M., 2002. Hypsometry and volume of the Arctic Ocean and its constituent seas. Geochemistry, Geophys. Geosystems 3, 1–18. https://doi.org/10.1029/2004GC000694

Lukashin, V.N., Shcherbinin, A.D., 2007. Hydrological Properties, Suspended Matter, and Particulate Fluxes in the Water Column of the Bear Island Trough. Mar. Geol. 47, 68–79. https://doi.org/10.1134/S0001437007010109

Luo, Y., Lippold, J., 2015. Controls on [231] Pa and [230] Th in the Arctic Ocean. Geophys. Res. Lett. n/a-n/a. https://doi.org/10.1002/2015GL064671

Moran, S.B., Hoff, J.A., Buesseler, K.O., Edwards, R.L., 1995. High precision 230Th and 232Th in the Norwegian Sea and Denmark by thermal ionization mass spectrometry. Geophys. Res. Lett. 22, 2589–2592.

Moran, S.B., Shen, C.C., Edmonds, H.N., Weinstein, S.E., Smith, J.N., Edwards, R.L., 2002. Dissolved and particulate 231Pa and 230Th in the Atlantic Ocean: Constraints on intermediate/deep water age, boundary scavenging, and 231Pa/230Th fractionation. Earth Planet. Sci. Lett. 203, 999–1014. https://doi.org/10.1016/S0012-821X(02)00928-7

Moran, S.B., Shen, C.C., Edwards, R.L., Edmonds, H.N., Scholten, J.C., Smith, J.N., Ku, T.L., 2005. 231Pa and 230Th in surface sediments of the Arctic Ocean: Implications for 231Pa/230Th fractionation, boundary scavenging, and advective export. Earth Planet. Sci. Lett. 234, 235–248. https://doi.org/10.1016/j.epsl.2005.02.016

Moran, S.B., Shen, C.C., Weinstein, S.E., Hettinger, L.H., Hoff, J.H., Edmonds, H.N., Edwards, R.L., 2001. Constraints on deep water age and particle flux in the Equatorial and South Atlantic Ocean based on seawater 231Pa and 230Th data. Geophys. Res. Lett. 28, 3437–3440. https://doi.org/10.1029/2001GL013339

Nelson, D.M., Tréguer, P., Brzezinski, M.A., Leynaert, A., Quéguiner, B., 1995. Production and dissolution of biogenic silica in the ocean: Revised global estimates, comparison with regional data and relationship to biogenic sedimentation. Global Biogeochem. Cycles 9, 359–372. https://doi.org/10.1029/95GB01070

Not, C., Brown, K., Ghaleb, B., Hillaire-Marcel, C., 2012. Conservative behavior of uranium vs. salinity in Arctic sea ice and brine. Mar. Chem. 130–131, 33–39. https://doi.org/10.1016/j.marchem.2011.12.005

Nowaczyk, N.R., Frederichs, T.W., Kassens, H., Norgaard-pedersen, N., Spielhagen, R.F., Stein, R., Weiel, D., 2001. Sedimentation rates in the Makarov Basin, central Arctic Ocean: A paleomagnetic and rock magnetic approach. Paleoceanography 16, 368–389.

Okubo, A., Takeda, S., Obata, H., 2013. Atmospheric deposition of trace metals to the western North Paci fi c Ocean observed at coastal station in Japan. Atmos. Res. 129–130, 20–32. https://doi.org/10.1016/j.atmosres.2013.03.014

Owens, S.A., Buesseler, K.O., Sims, K.W.W., 2011. Re-evaluating the 238U-salinity relationship in seawater: Implications for the 238U-234Th disequilibrium method. Mar. Chem. 127, 31–39. https://doi.org/10.1016/j.marchem.2011.07.005

Pavia, F., Anderson, R., Vivancos, S., Fleisher, M., Lam, P., Lu, Y., Cheng, H., Zhang, P., Lawrence Edwards, R., 2018. Intense hydrothermal scavenging of 230Th and 231Pa in the deep Southeast Pacific. Mar. Chem. 201, 212–228. https://doi.org/10.1016/j.marchem.2017.08.003

Pfirman, S., Thiede, J., 1987. Lithogenic sediment on Arctic pack ice: Potential aeolian flux and contribution to deep sea sediments, in: Paleoclimatology and Paleometeorology: Modern and Past Patterns of Global Atmospheric Transport. pp. 463–493.

Rijkenberg, M.J.A., Slagter, H.A., Rutgers van der Loeff, M., van Ooijen, J., Gerringa, L.J.A., 2018. Dissolved Fe in the Deep and Upper Arctic Ocean With a Focus on Fe Limitation in the Nansen Basin. Front. Mar. Sci. 5, 1–14. https://doi.org/10.3389/fmars.2018.00088

Roy-Barman, M., 2009. Modelling the effect of boundary scavenging on Thorium and Protactinium profiles in the ocean. Biogeosciences 6, 7853–7896. https://doi.org/10.5194/bgd-6-7853-2009

Rudels, B., 2009. Arctic ocean circulation. Finnish Institute of Marine Research, Helsinki, Finland, pp. 211–225.

988   Rutgers Van Der Loeff, M., Matthew, A., Willard, S., 2018. Radium Isotopes Across the Arctic
989   Ocean Show Time Scales of Water Mass Ventilation and Increasing Shelf Inputs. J.
990   Geophys. Res. Ocean. 123.

991   Rutgers van der Loeff, M.M., Berger, G.W., 1993. Scavenging of 230Th and 231Pa near the
992   antarctic polar front in the South Atlantic. Deep. Res. Part I 40, 339–357.
993   https://doi.org/10.1016/0967-0637(93)90007-P

994   Rutgers Van Der Loeff, M.M., Boudreu, B.P., 1997. the effect of resuspension on chemical
995   exchanges at the sediment-water interface in the deep sea: a modelling and natural
996   radiotracer approach. J. Mar. Syst. 11, 305–342.

997   Schlosser, P., Kromer, B., Ekwurzel, B., Bönisch, G., McNichol, A., Schneider, R., von
998   Reden, K., Östlund, H.G., Swift, J.H., 1997. The first trans-Arctic 14C section:
999   comparison of the mean ages of the deep waters in the Eurasian and Canadian basins
1000   of the Arctic Ocean. Nucl. Instruments Methods Phys. Res. Sect. B Beam Interact. with
1001   Mater. Atoms 123, 431–437. https://doi.org/10.1016/S0168-583X(96)00677-5

1002   Scholten, J.C., Fietzke, J., Mangini, A., Garbe-Schönberg, C.D., Eisenhauer, A., Schneider,
1003   R., Stoffers, P., 2008. Advection and scavenging: Effects on 230Th and 231Pa
1004   distribution off Southwest Africa. Earth Planet. Sci. Lett. 271, 159–169.
1005   https://doi.org/10.1016/j.epsl.2008.03.060

1006   Scholten, J.C., Rutgers van der Loeff, M.M., Michel, A., 1995. Distribution of 230Th and
1007   231Pa in the water column in relation to the ventilation of the deep Arctic basins. Deep.
1008   Res. Part II 42, 1519–1531. https://doi.org/10.1016/0967-0645(95)00052-6

1009   Smith, J.N., Moran, S.B., Macdonald, R.W., 2003. Shelf-basin interactions in the Arctic
1010   Ocean based on 210Pb and Ra isotope tracer distributions. Deep. Res. Part I
1011   Oceanogr. Res. Pap. 50, 397–416. https://doi.org/10.1016/S0967-0637(02)00166-8

1012   Tanhua, T., Jones, E.P., Jeansson, E., Jutterstro, S., Jr, W.M.S., Wallace, D.W.R.,
1013   Anderson, L.G., 2009. Ventilation of the Arctic Ocean: Mean ages and inventories of
1014   anthropogenic CO2 and CFC-11. J. Geophys. Res. 114, 1–11.
1015   https://doi.org/10.1029/2008JC004868

1016   Valk, O., Rutgers van der Loeff, M.M., Geibert, W., Gdaniec, S., Rijkenberg, M.J.A., Moran,
1017   S.B., Lepore, K., Edwards, R.L., Lu, Y., Puigcorbé, V., 2018. Importance of
1018   hydrothermal vents in scavenging removal of ^{230} Th in the Nansen Basin. Geophys. Res.
1019   Lett. 1–10. https://doi.org/10.1029/2018GL079829

1020   Venchiarutti, C., Roy-Barman, M., Freydier, R., Van Beek, P., Souhaut, M., Jeandel, C.,
1021   2011a. Influence of intense scavenging on Pa-Th fractionation in the wake of Kerguelen
1022   Island (Southern Ocean). Biogeosciences 8, 3187–3201. https://doi.org/10.5194/bg-8-
1023   3187-2011

1024   Venchiarutti, C., van der Loeff, M.R., Stimac, I., 2011b. Scavenging of 231Pa and thorium
1025   isotopes based on dissolved and size-fractionated particulate distributions at Drake
1026   Passage (ANTXXIV-3). Deep. Res. Part II Top. Stud. Oceanogr. 58, 2767–2784.
1027   https://doi.org/10.1016/j.dsr2.2010.10.040

1028   Wassmann, P., Vernet, M., Mitchell, B., Rey, F., 1990. Mass sedimentation of *Phaeocystis*
1029   *pouchetii* in the Barents Sea. Mar. Ecol. Prog. Ser. 66, 183–195.
1030   https://doi.org/10.3354/meps066183

1031

1032

Figures and tables

1034

1035   **Figure 1**: Samples for the analysis of dissolved and particulate ^{231}Pa, ^{230}Th and ^{232}Th were
1036   collected at 9 stations along the GEOTRACES GN04 section in the Arctic Ocean. Crossed
1037   symbols denote sampling for particulate and dissolved samples and non-crossed points are
1038   stations which were sampled for the analysis of dissolved concentrations.

1039

1040   **Figure 2**: Dissolved concentrations of ^{231}Pa$_{xs}$, ^{230}Th$_{xs}$ and ^{232}Th for shelf stations (upper
1041   panel) and deep stations (lower panel). Diamonds: Nansen Basin, squares: Amundsen
1042   basin, triangles: Makarov Basin and circles: shelf stations.

1043

1044   **Figure 3**: Particulate concentrations of ^{231}Pa$_{xs}$, ^{230}Th$_{xs}$ and ^{232}Th for shelf stations (upper
1045   panel) and deep stations (lower panel). Diamonds: Nansen Basin, triangles: Makarov Basin
1046   and circles: shelf stations

1047

1048   **Figure 4**: Pa-Th Fractionation factors. Diamonds: Nansen Basin, triangles: Makarov Basin
1049   and circles: shelf stations.

1050   **Figure 5**: Depth profiles of (a) the particulate/total ratios of ^{231}Pa$_{xs}$ and (b) particulate/total
1051   ratios for ^{230}Th$_{xs}$. Diamonds: Nansen Basin, triangles: Makarov Basin and circles: shelf
1052   stations.

1053   **Figure 6**: Schematic representation of the boundary scavenging profile model: the margin and
1054   open ocean boxes exchange a total flux of water (F). Vertical mixing is neglected. Particles are
1055   introduced in the surface waters of the ocean margin and interior and at all depths in the margin
1056   box (bent arrows). Particles are then transported by currents between the margin and ocean
1057   interior.

1058

1059   **Figure 7**: Boundary scavenging model outputs. Modelled profiles of (a and d): particle
1060   abundance and the ^{230}Th particulate fraction, (b and e): dissolved and particulate ^{230}Th$_{xs}$ and
1061   c and f): dissolved and particulate ^{231}Pa$_{xs}$ in comparison with measured data obtained at
1062   station 32 (margin) and 50 (interior). Pink open diamonds (st 32) and orange diamonds (st
1063   50) represent measured data while the pink lines represent the margin model and orange
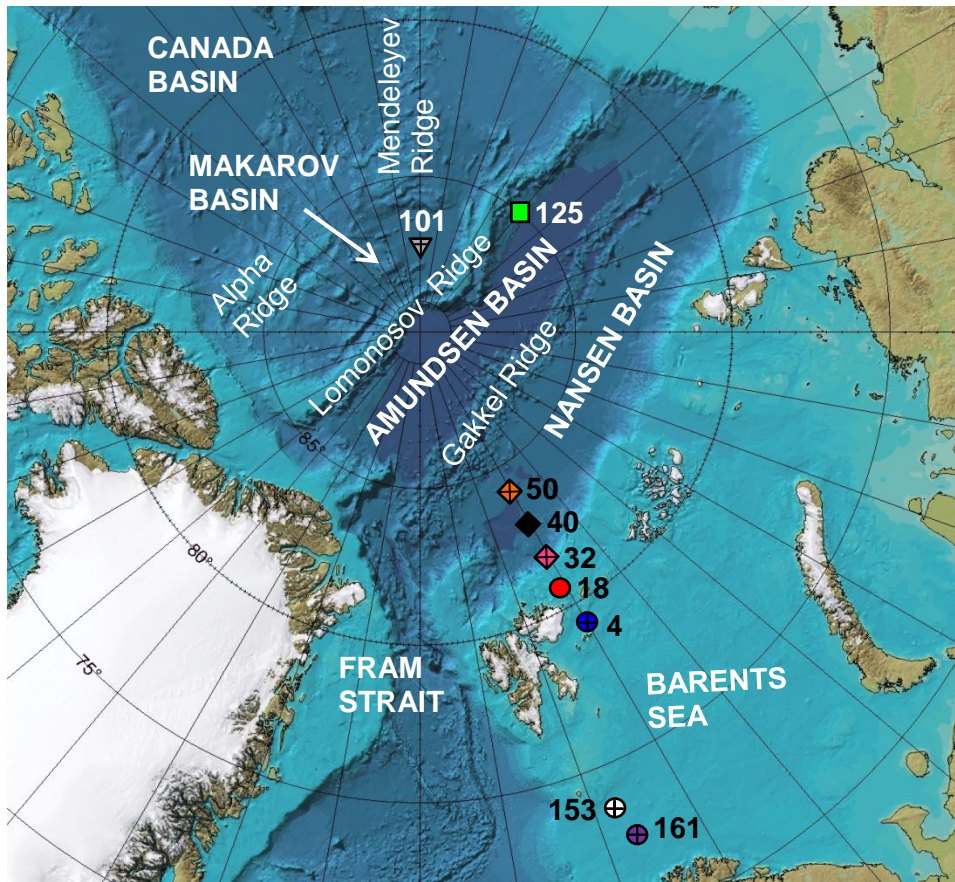1064   lines represent the interior ocean model.

1065

1066   **Figure 8**: Dissolved ^{231}Pa$_{xs}$ versus DSi measured during PS94 (Van Ooijen et al., 2016).
1067   Diamonds: Nansen Basin, squares: Amundsen basin, triangles: Makarov Basin and circles:
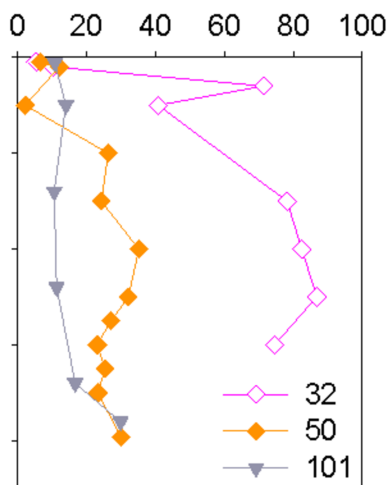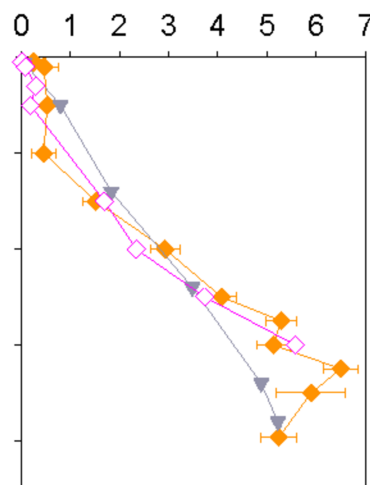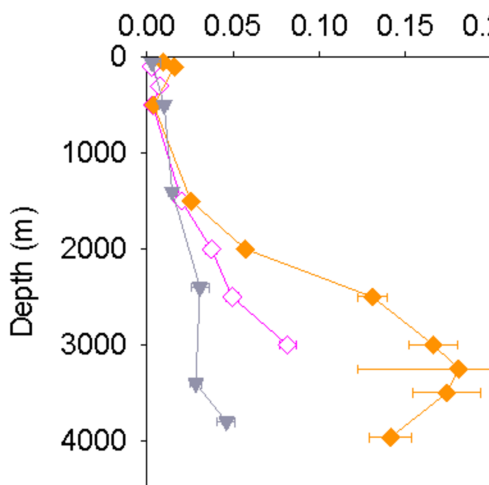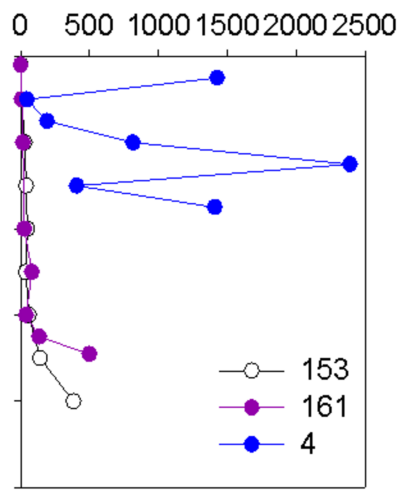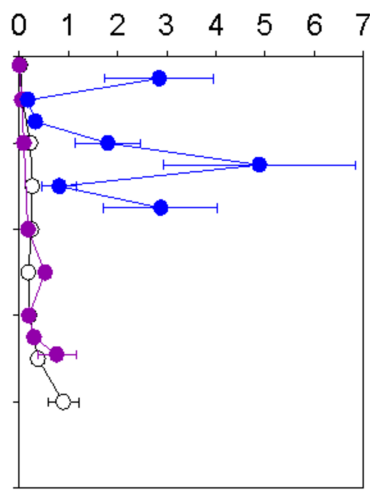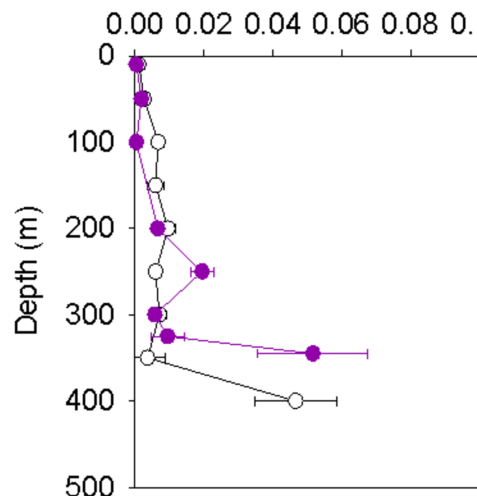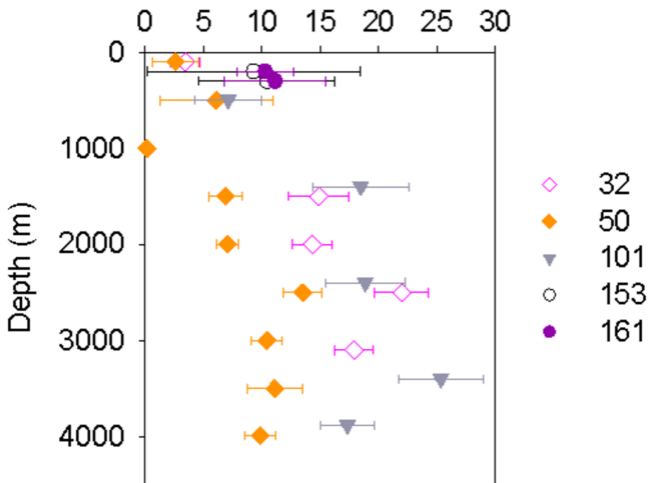1068   shelf stations.

1069

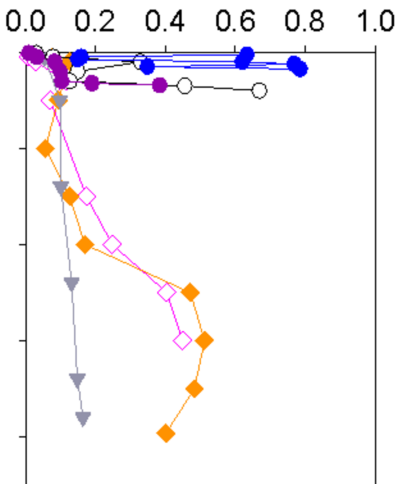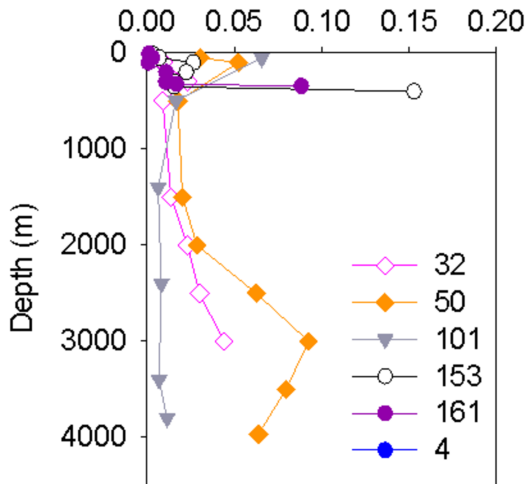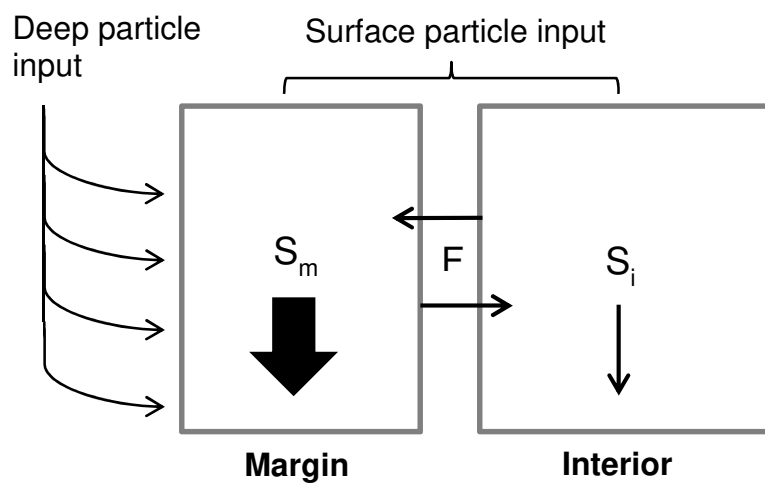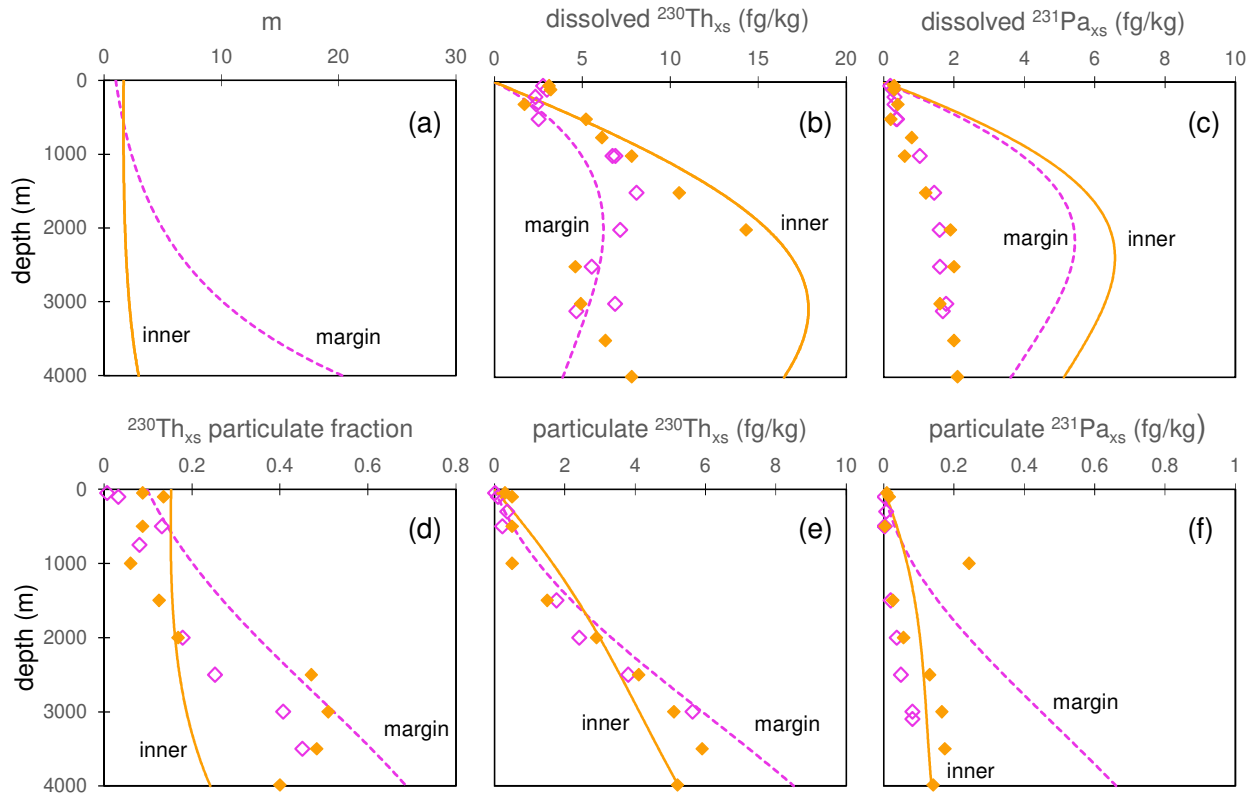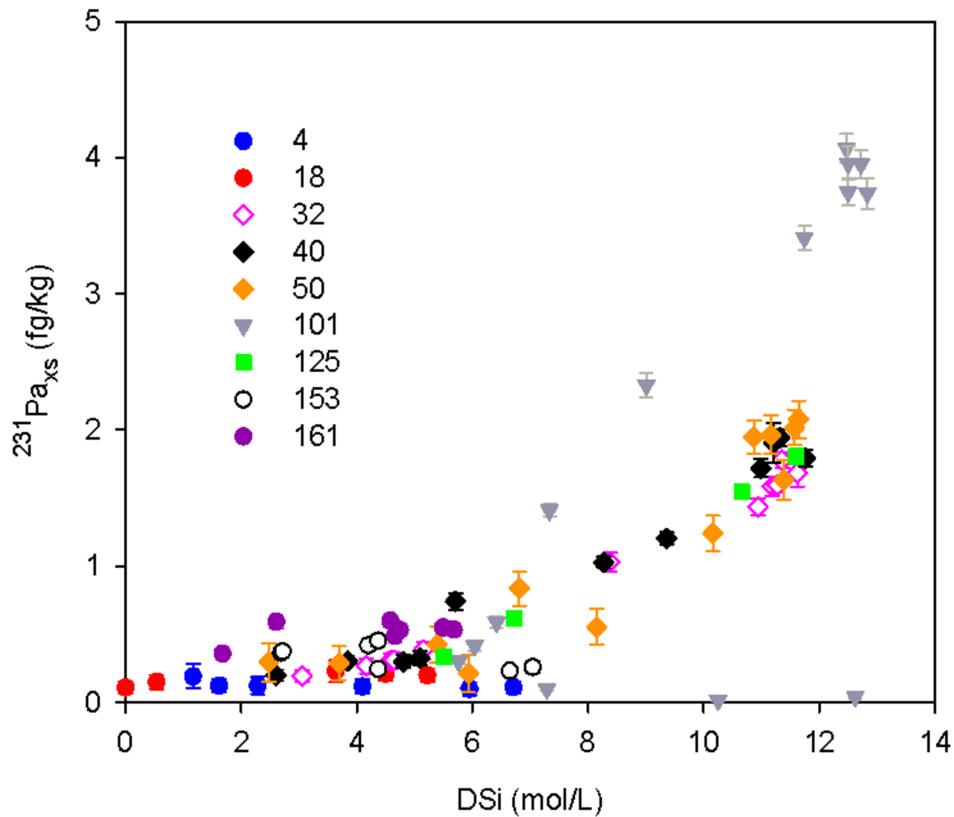1070   **Table 1:** Parameters of the Boundary scavenging profile model

1071

1072

Table 1. Parameters of the Boundary scavenging profile model

Parameter	Ocean interior	Ocean margin
V (m^3)	6.5 x 10^{15}	1.5 x 10^{15}
F (m^3/y)	1.3 x 10^{14}	1.3 x 10^{14}
т (y)	50	10
k	0.02	0.1
S (m/y)	300	600
K^{230}Th	0.11	0.11
K^{231}Pa	0.0075	0.0075
P^{230}Th (fg/m^3/y)	0.056	0.056
P^{231}Pa (fg/m^3/y)	0.025	0.025
µ (y^{-1})		0.5
m (0)	1.5	1